

POLITECNICO DI TORINO

Master's Degree in Civil Engineering



Master's Degree Thesis

Cyclic Non-linear Analysis of Complex Reinforced Concrete
Structures with GLRC_HEGIS Model

Supervisors

Prof. Rosario CERAVOLO

Dir. HDR Silvano ERLICHER

Ph.D. Miquel HUGUET AGUILERA

Candidate

Michele MASSARELLA

Academic year: 2019/2020

Summary

The following master's thesis was written during a period of foreign mobility, with a duration of 5 months, which was spent at Egis, a French group leader in the engineering sector. In particular, the internship was carried out in the Egis Industries (nuclear department of EGIS group), within the EAS (Egis Advanced Solutions) team. The internship aimed at validating GLRC_HEGIS nonlinear constitutive model developed by Miquel Huguet Aguilera for the software Code_Aster, by means of a several simulations aimed at reproducing the behaviour of real case studies. This constitutive law is able to reproduce the main nonlinear phenomena that characterise the behaviour of RC (reinforced concrete) elements: concrete damage, concrete cracking, bond-slip stress and yielding of steel reinforcement bars. The validation of the model has been carried out through three main analyses: (i) comparison with experimental results of reinforced concrete walls subjected to horizontal cyclic loads in plane shear, (ii) the comparison with other non-linear global models available in Code_Aster and (iii) comparison with experimental results of reinforced concrete elements subjected to pure out-of-plane bending. The first considered experimental test includes the four walls designed and tested in the framework of the French national research project CEOS.fr (Behaviour and Assessment of Special Structures. Cracking - Shrinkage). Shear-wall specimens were designed in order to simulate the behaviour of the nuclear power plant walls submitted to the seismic action. The four walls are subjected to horizontal cyclic loading in plane shear (reversing for three walls and non-reversing for one) and differ from each other or by the strength class of the concrete used, or by the amount of reinforcement or by the type of load applied. The numerical results obtained were compared with the available experimental ones, in terms of force-displacement curves and crack opening on the walls surface. Then, the GLRC_HEGIS global model was compared to other global models for RC plates available in Code_Aster (GLRC_DM, DHRC and EIB) already implemented in Code_Aster and has been analysed the case of cyclic pure flexion test. In particular, the behaviour of a reinforced concrete plate subjected to constant cyclic bending moment was studied, implementing the results already obtained with two different load cases. At first, the number of cycles was increased from one to six and subsequently an increasing moment was applied. The comparison with the other models mainly concerned the energy dissipated during the load cycles and the applied rotation-moment curves. To extend the results obtained so far, the model was used to simulate an experimental test of a three-point RC beam subjected to pure bending. The numerical results have been compared with the experimental ones and important conclusions have been reached. In particular, by studying both behaviours (membrane and flexural) it is noted that the general behaviour of the model is governed mainly by the concrete damage. In fact, for all the models the same non-linear parameters were used except those relating to the damage to the concrete. That means that concrete damage is the only phenomena that behaves differently in membrane and in bending solicitations. This aspect makes it possible to standardize the model and further eliminate the small uncertainty that governs the choice of parameters that must be used.

*Alla mia famiglia,
ai miei amici
e a tutte le persone che credono in me.*

Acknowledgements

Firstly I would thank Egis Industries and Politecnico di Torino for allowing me to carry out these months of internship in which the following master thesis has been prepared. In particular a special thanks to Director Silvano Erlicher and Miquel Huguet-Aguilera, my company supervisors, who have always encouraged and followed me in my work. I especially thank my academic tutor Prof. Rosario Ceravolo for supporting me during my thesis period. I thank all the guys who have always helped me on this path with technical advice and suggestions, in particular a special thank you to Olivier, Jean, Thibaut, David, Giuseppe and Nicola. Thank you again all the guys of Egis Industries who welcomed me right away on this adventure and with whom I shared pleasant moments inside and outside the work environment. An infinite thanks to my family who has always supported me during these years and to all my friends, constant and indispensable presence to better face any challenge.

Table of Contents

List of Tables	8
List of Figures	9
Acronyms	12
1 INTRODUCTION	13
2 GLRC_HEGIS model	14
2.1 Helmholtz free energy surface density [3]	14
2.1.1 Helmholtz free energy surface density as a function of the state variables	14
2.1.2 Thermodynamic forces	16
2.2 Local constitutive laws	16
2.2.1 Concrete damage	16
2.2.2 Cracking of the concrete	18
2.2.3 Steel-concrete bond-slip	22
2.2.4 Yielding of steel reinforcement bars	23
2.3 Numerical implementation [2]	24
2.3.1 DKTG Finite Element	24
3 CEOS.FR	25
3.1 Experimental test description [7, 8, 9, 10]	25
3.1.1 Experimental test results [11]	27
3.2 Numerical Model	29
3.2.1 Non-linear analysis	30
3.3 Comparison between experimental and numerical results	32
3.3.1 Crack opening	32
3.3.2 Envelope curves	39
3.3.3 Crack pattern	39
4 CODE_ASTER TESTS	47
4.1 Cyclic pure flexion test [12]	47
4.1.1 Constant rotation over time	49
4.1.2 Incremental rotation over time	51

5	THREE-POINT BENDING TEST ON RC BEAM	53
5.1	Experimental test description	53
5.1.1	Experimental test results	55
5.2	Numerical model	56
5.2.1	Non-linear analysis	56
5.3	Comparison between experimental and numerical results	57
5.4	Study of mesh sensitivity	59
5.5	Comparison with membrane behaviour model	61
6	CONCLUSION	66
A		67
B		69

List of Tables

3.1	Main characteristics of the specimens.	26
3.2	GLRC_HEGIS parameters for CEOS.fr RC walls.	31
4.1	GLRC_HEGIS parameters for CAS_TEST.	48
5.1	Mechanical characteristic of the concrete.	54
5.2	Mechanical characteristic of the steel.	54
5.3	GLRC_HEGIS parameters for RC beam.	56
5.4	GLRC_HEGIS parameters for RC beam (third model).	61
B.1	Parameters of GLRC_HEGIS model.	69
B.2	Internal variables of the GLRC_HEGIS model.	70

List of Figures

2.1	Uniaxial concrete response with damage evolution.	17
2.2	Displacement discontinuity at cracks.	18
2.3	Second crack in a RC panel: cracked RC panel geometry and relative orientation between the two cracks.	19
2.4	Relation between normal concrete stress at cracks g_n and crack opening w_n	20
2.5	Aggregate interlock considered by Walraven.	20
2.6	Experimental cyclic aggregate interlock test vs. analytical results of Contact Density Model [5].	21
2.7	Gambanova aggregate interlock law [6].	21
2.8	Tangential-to crack concrete stress at cracks g_t as a function of the tangential crack displacement w_t	22
2.9	Transformation from crack openings to steel-concrete slip in (a) x direction and (b) y direction.	23
2.10	Typical force-displacement curve for a RC beam with a displacement-controlled test.	23
2.11	Relationship between real and reference DKQG and DKTG elements.	24
3.1	Dimensions of the specimen [7]	25
3.2	Steel frame of the specimen [7]	26
3.3	Section in the middle of steel frame and of the specimen (a) and reinforcement and part of formwork (b) [7].	26
3.4	Measured load time histories: reversing cycling load (left), non reversing cycling load (right).	27
3.5	Arrangement of sensors for walls A, B, C and D respectively.	27
3.6	Experimental global force-displacement curves.	28
3.7	Experimental crack orientation.	28
3.8	FE model of the RC walls (a) and 3D visualization (b).	29
3.9	Real boundary conditions.	29
3.10	Modelled boundary conditions.	30
3.11	Experimental vs. numerical global force-displacement curves.	32
3.12	Experimental vs. numerical crack opening for wall A at sensors D18, D19 and D20.	33
3.13	Experimental vs. numerical crack opening for wall B at sensors D1 to D11.	35
3.14	Experimental vs. numerical crack opening for wall C at sensors D5, D6 and D7.	36
3.15	Experimental vs. numerical crack opening for wall D at sensors D1 to D8.	38
3.16	Experimental vs. numerical envelope curves.	39
3.17	Experimental vs. numerical crack pattern at $F = \pm 900$ kN.	40
3.18	Experimental vs. numerical crack pattern at $F = \pm 1200$ kN.	40
3.19	Experimental vs. numerical crack pattern at $F = \pm 1500$ kN.	41

3.20	Experimental vs. numerical crack pattern at $F = \pm 1800$ kN.	41
3.21	Experimental vs. numerical crack pattern at $F = \pm 2100$ kN.	42
3.22	Experimental vs. numerical crack pattern at $F = \pm 2400$ kN.	42
3.23	Experimental vs. numerical crack pattern at $F = \pm 2700$ kN.	43
3.24	Experimental vs. numerical crack pattern at $F = \pm 3000$ kN.	43
3.25	Experimental vs. numerical crack pattern at $F = \pm 3300$ kN.	44
3.26	Experimental vs. numerical crack pattern at $F = \pm 3600$ kN.	44
3.27	Experimental vs. numerical crack pattern at $F = \pm 3900$ kN.	45
3.28	Experimental vs. numerical crack pattern at $F = \pm 4200$ kN.	45
3.29	Numerical values of the residual cracks after $F = \pm 4200$ kN.	46
4.1	Geometry of the considered RC plate.	47
4.2	FE model and boundary conditions.	48
4.3	Loading history with constant rotation.	49
4.4	Moment-rotation comparison.	49
4.5	Dissipated energy comparison.	50
4.6	GLRC_HEGIS: Crack opening evolution (a) and dissipated energy components.	50
4.7	Loading history with constant rotation.	51
4.8	GLRC_HEGIS: Moment-rotation (a) and dissipated energy (b) comparison.	51
4.9	GLRC_HEGIS: Crack opening evolution (a) and dissipated energy components (b).	52
5.1	Test layout.	53
5.2	Beam's section (a) and sensors arrangement (b).	54
5.3	Measured load time history.	54
5.4	Global experimental force-displacement curves at half (a), one quarter and three-fourth of the length (b).	55
5.5	Experimental steel deformation given by sensors J1-J6.	55
5.6	FE model of the RC beam.	56
5.7	Global experimental vs. numerical force-displacement curves at half (a), one quarter and three-fourth of the length (b).	57
5.8	Experimental vs. numerical steel deformation given by sensors J1-J6.	57
5.9	Trend of the main internal variables and dissipated energy components.	58
5.10	Second FE model of the beam.	59
5.11	Global experimental vs. numerical force-displacement curves at half (a), one quarter and three-fourth of the length (b) for the second model.	59
5.12	Experimental vs. numerical steel deformation given by sensors J1-J6 for the second model.	60
5.13	Trend of the main internal variables (a) and dissipated energy components (b) for the second model.	60
5.14	Third FE model of the RC beam.	62
5.15	Global experimental vs. numerical force-displacement curves at half (a), one quarter and three-fourth of the length (b) for the third model.	62
5.16	Experimental vs. numerical steel deformation given by sensors J1-J6 for the third model.	63
5.17	Trend of the main internal variables (a) and dissipated energy components (b).	63
5.18	Experimental vs. numerical crack pattern at $F = 90$ kN (Cycle 5).	64
5.19	Experimental vs. numerical crack pattern at $F = 150$ kN (Cycle 6).	64
5.20	Experimental vs. numerical crack pattern at $F = 185$ kN (Cycle 7).	64
5.21	Numerical values of the crack openings at the end of test.	65

Acronyms

DHRC

Dissipative Homogenised Reinforced Concrete

DKTG

Discrete Kirchhoff Triangle Generalized

EIB

Endommagement Isotrope Beton

FE

Finite Elements

GLRC

Global Reinforced Concrete Models

RC

Reinforced Concrete

Chapter 1

INTRODUCTION

Egis is a major international group in the construction engineering and mobility services sectors whose unique global service range encompasses infrastructure consulting, engineering and operation. Through its capacity for innovation, it responds to the climate emergency and to the greatest challenges of our time by offering solutions and acknowledged know-how in the areas of transportation and mobility, sustainable city construction, buildings, water, the environment and energy.

The need for innovation in non-linear calculations and the need to have models capable of describing their behaviour when submitted to seismic action, led Egis to develop a non-linear global model capable of simulating the global behaviour of reinforced concrete shell elements under cyclic load. During my internship I had the opportunity to learn and use this model and thus to expand the company's knowledge about it. In the first period of my internship I analysed and subsequently improved the results obtained by one of my predecessors on the study of a reinforced concrete plate subjected to horizontal cyclic loads within the French CEOS.fr program in order to simulate the behaviour of the nuclear power plant walls submitted to the seismic action. Subsequently, the study was extended to analyse the behaviour of the model in the case of pure bending: at first the model was compared with other non-linear global model available in Code_Aster through simple tests made available directly by the code developer, extending the results already obtained to longer and increased loading cycles. Afterwards, the comparison was made with a three-point experimental bending test emphasizing the behaviour of the model in the case of pure bending and analysing how each individual non-linear parameter affects it.

The finite element code used was developed by EDF and is mainly used for the analysis of structures and thermomechanics for studies and research. Code_Aster [1] is an open source free software and therefore it allows to add / develop new functions and for this reason it was possible to implement the GLRC_HEGIS model in it. It is also developed in the Python environment and this allows to operate with greater ease especially in the post processing phase.

Chapter 2

GLRC_HEGIS model

GLRC_HEGIS is a global constitutive model developed by Miquel HUGUET-AGUILERA [2] in order to describe the response of reinforcement concrete buildings submitted to seismic actions. To limit the computational time it's necessary to use plate and shell element to model concrete and reinforcement steel bars (global modelling). In order to use the aforementioned model, it is necessary to define a series of linear and non-linear parameters capable of taking into account all the phenomena considered in the model.

In particular, this model currently takes into consideration four non-linear phenomena:

- Concrete damage
- Cracking of the concrete
- Steel-concrete bond slip
- Yielding of steel reinforcement bars

The global behaviour of the model is described by 18 internal variables that become 47 if we consider the parametric variables (top and bottom layer), the variables related to energy dissipation and those of post-treatment. The all intern variables are listed in Appendix B.

The constitutive model is formulated in the framework of Thermodynamics of Irreversible Processes. At the beginning it has been obtained using an analytical homogenization of a RC panel submitted to in-plane forces considering only one crack direction; afterwards, the model has been extended to take into account a second crack direction and finally out-of-plane bending moments (Figure 2.3).

The Helmholtz free energy surface density and the phenomena taken into consideration by the model will be described below.

2.1 Helmholtz free energy surface density [3]

2.1.1 Helmholtz free energy surface density as a function of the state variables

The Helmholtz free energy surface density defines the elastic part of the material behaviour and depends on the state variables of the model:

- Observable variables, which define the linear elastic behaviour:

- The generalized membrane strain $\boldsymbol{\epsilon}$, composed of three components ϵ_{xx} , ϵ_{yy} and ϵ_{xy}
- The generalized curvature $\boldsymbol{\kappa}$, composed of three components κ_{xx} , κ_{yy} and κ_{xy}
- Internal variables, which describe the non-linear behaviour of the model:
 - The crack displacement $\underline{w} = (w_n, w_t)$ in the normal (crack opening) w_n and in the tangential w_t directions with respect to the crack:
 - * For the first family of cracks of the top layer: \underline{w}_1^t
 - * For the second family of cracks of the top layer: \underline{w}_2^t
 - * For the first family of cracks of the bottom layer: \underline{w}_1^b
 - * For the second family of cracks of the bottom layer: \underline{w}_2^b
 - The steel concrete inelastic slip $\underline{v}^p = (v_x^p, v_y^p)$ in the x v_x^p and y v_y^p reinforcement directions:
 - * For the top layer: \underline{v}^{pt}
 - * For the bottom layer: \underline{v}^{pb}
 - The steel plastic strain $\underline{\epsilon}^{ps} = (\epsilon_x^{ps}, \epsilon_y^{ps})$ in the x ϵ_x^{ps} and y ϵ_y^{ps} reinforcement directions:
 - * For the top layer: $\underline{\epsilon}^{pst}$
 - * For the bottom layer: $\underline{\epsilon}^{psb}$
 - Concrete damage variable d :
 - * For the top layer: d^t
 - * For the bottom layer: d^b

Thus a total of 18 internal scalar variables, together with the observable strain variables, define the Helmholtz free energy surface density, which can be expressed as the sum of three different terms:

$$\psi^0 = \psi^{lin}(\boldsymbol{\epsilon}, \boldsymbol{\kappa}; \underline{w}_1^t, \underline{w}_2^t, \underline{w}_1^b, \underline{w}_2^b, \underline{\epsilon}^{pst}, \underline{\epsilon}^{psb}, d^t, d^b) + \psi^{nl}(\underline{w}_1^t, \underline{w}_2^t, \underline{w}_1^b, \underline{w}_2^b, \underline{v}^{pt}, \underline{v}^{pb}, \underline{\epsilon}^{pst}, \underline{\epsilon}^{psb}, d^t, d^b) \quad (2.1)$$

with ψ^{lin} depending on the observable variables:

$$\psi^{lin} = \frac{1}{2} \begin{pmatrix} \boldsymbol{\epsilon} \\ \boldsymbol{\kappa} \end{pmatrix} : \begin{pmatrix} \mathbb{A}^{mm} & \mathbb{A}^{mf} \\ \mathbb{A}^{mf} & \mathbb{A}^{ff} \end{pmatrix} : \begin{pmatrix} \boldsymbol{\epsilon} \\ \boldsymbol{\kappa} \end{pmatrix} + \sum_{\beta} \left(- \sum_{\gamma} \begin{pmatrix} \boldsymbol{\epsilon} \\ \boldsymbol{\kappa} \end{pmatrix} : \begin{pmatrix} \mathbb{B}_{\gamma}^{\beta m} \\ \mathbb{B}_{\gamma}^{\beta f} \end{pmatrix} \cdot \underline{w}_{\gamma}^{\beta} - \begin{pmatrix} \boldsymbol{\epsilon} \\ \boldsymbol{\kappa} \end{pmatrix} : \begin{pmatrix} \mathbb{C}_{\gamma}^{\beta m} \\ \mathbb{C}_{\gamma}^{\beta f} \end{pmatrix} \cdot \underline{\epsilon}^{ps\beta} \right) \quad (2.2)$$

and $\psi^{nl,t}$ and $\psi^{nl,b}$ determining the coupling between the internal variables:

$$\psi^{nl,\beta} = \sum_{\gamma} \frac{1}{2} \underline{w}_{\gamma}^{\beta} \cdot \mathbf{D}_{\gamma}^{\beta} \cdot \underline{w}_{\gamma}^{\beta} + \frac{1}{2} \underline{v}^{p\beta} \cdot \mathbf{E}^{\beta} \cdot \underline{v}^{p\beta} + \frac{1}{2} \underline{\epsilon}^{ps\beta} \cdot \mathbf{F}^{\beta} \cdot \underline{\epsilon}^{ps\beta} - \sum_{\gamma} \underline{w}_{\gamma}^{\beta} \cdot \mathbf{G}_{\gamma}^{\beta} \cdot \underline{v}^{p\beta} + \underline{w}_1^{\beta} \cdot \mathbf{H}^{\beta} \cdot \underline{w}_2^{\beta} \quad (2.3)$$

where $\gamma = 1,2$ denotes the first and second family of cracks for each layer. It is remarked that:

- The fourth order tensor \mathbb{A}^{mm} , \mathbb{A}^{mf} and \mathbb{A}^{ff} depend on d^t and d^b
- The three order tensors $\mathbb{B}_{\gamma}^{\beta m}$ and $\mathbb{B}_{\gamma}^{\beta f}$ depend on d^{β}
- The two order tensors $\mathbf{D}_{\gamma}^{\beta}$, \mathbf{E}^{β} , $\mathbf{G}_{\gamma}^{\beta}$ and \mathbf{H}^{β} depend on d^{β}

and all of them, together with the three order tensors $\mathbb{C}_\gamma^{\beta m}$ and $\mathbb{C}_\gamma^{\beta f}$ and the two order tensors \mathbf{F}^β are determined uniquely from:

- Geometrical properties of the section;
- Material elastic properties;
- Crack pattern geometry;

2.1.2 Thermodynamic forces

The constitutive law of the model is the relationship between the generalized efforts:

- in-plane stress resultant $\mathbf{N} = (N_{xx}, N_{yy}, N_{xy})$
- out-of-plane generalized bending moment $\mathbf{M} = (M_{xx}, M_{yy}, M_{xy})$

and the observable variables: the generalized membrane strain $\boldsymbol{\epsilon}$ and the generalized curvature $\boldsymbol{\kappa}$. By definition, this relationship is obtained by derivation of the Helmholtz free energy surface density:

$$\begin{aligned} \mathbf{N} &= \frac{\partial \psi^0}{\partial \boldsymbol{\epsilon}} = \mathbb{A}^{mm} : \boldsymbol{\epsilon} + \mathbb{A}^{mf} : \boldsymbol{\kappa} - \sum_{\beta} \left(\sum_{\chi} \mathbb{B}_{\chi}^{\beta m} \cdot \underline{w}_{\chi}^{\beta} + \mathbb{C}^{\beta m} \cdot \underline{\underline{\epsilon}}^{ps\beta} \right) \\ \mathbf{M} &= \frac{\partial \psi^0}{\partial \boldsymbol{\kappa}} = \mathbb{A}^{mf} : \boldsymbol{\epsilon} + \mathbb{A}^{ff} : \boldsymbol{\kappa} - \sum_{\beta} \left(\sum_{\chi} \mathbb{B}_{\chi}^{\beta f} \cdot \underline{w}_{\chi}^{\beta} + \mathbb{C}^{\beta f} \cdot \underline{\underline{\epsilon}}^{ps\beta} \right) \end{aligned} \quad (2.4)$$

2.2 Local constitutive laws

The evolution of the 18 scalar internal variables presented in the previous section is governed by 18 scalar threshold equations depending on the thermodynamic forces of the model. These threshold functions are the description of each of the four non-linear physical phenomena retained for the description of the RC plates behaviour: concrete cracking, concrete damage, steel yielding and the relative steel-concrete slip.

2.2.1 Concrete damage

Concrete damage is considered as isotropic and it is introduced as an internal scalar positive variable, d which can evolve only at high stress states associated to compression. Concrete Young's modulus E_c is reduced through a decreasing convex function $\zeta(d)$:

$$E_c(d) = E_c \zeta(d) \quad (2.5)$$

Concrete is modelled using an isotropic elastic damage constitutive law characterised by a stiffness tensor $\mathbb{C}_c(d)$, defined by the Young's modulus E_c , the Poisson's ratio ν_c and the decreasing convex function $\zeta(d)$. The relationship between concrete membrane stress $\boldsymbol{\sigma}^c$ and the plane components of the strain tensor $\boldsymbol{\epsilon}^c$ is given by:

$$\boldsymbol{\sigma}^c = \mathbb{C}_c(d) : \boldsymbol{\epsilon}^c \quad (2.6)$$

which can be also expressed as:

$$\begin{pmatrix} \sigma_{xx}^c \\ \sigma_{yy}^c \\ \sigma_{xy}^c \end{pmatrix} = \frac{E_c \zeta(d)}{1 - \nu_c^2} \begin{pmatrix} 1 & \nu_c & 0 \\ \nu_c & 1 & 0 \\ 0 & 0 & \frac{1 - \nu_c}{2} \end{pmatrix} \cdot \begin{pmatrix} \epsilon_{xx}^c \\ \epsilon_{yy}^c \\ \epsilon_{xy}^c \end{pmatrix} \quad (2.7)$$

The chosen convex decreasing function is defined as:

$$\zeta(d) = \frac{1 + \gamma_d d}{1 + d} \quad (2.8)$$

And was inspired by the constitutive models GLRC_DM et DHRC. One of the properties of this function is that it tend towards infinity to γ_c when d approaches $+\infty$:

$$\lim_{d \rightarrow +\infty} \zeta(d) = \gamma_c \quad (2.9)$$

The damage function used $\zeta(d)$ assures a damage evolution phase with a constant tangent slope $\gamma_d E_c$ and a bilinear behaviour of the concrete with:

$$\sigma^c = \begin{cases} \epsilon^c E_c & \text{for } \sigma^c \leq \sigma_d \\ \sigma_d + \left(\epsilon^c - \frac{\sigma_d}{E_c} \right) \gamma_d E_c & \text{for } \sigma^c > \sigma_d \end{cases} \quad (2.10)$$

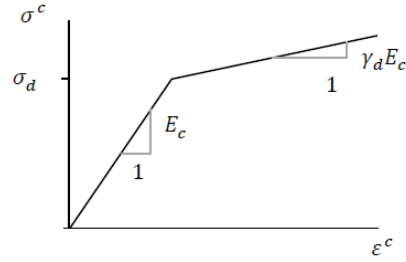


Figure 2.1: Uniaxial concrete response with damage evolution.

2.2.2 Cracking of the concrete

For the definition of cracks in RC panels, the crack opening w_n and the tangential crack displacement w_t are necessary in order to define the complete concrete displacement fields at crack. As you can see in the Figure 2.2 the crack displacement vector is defined as $\underline{w} = (w_n, w_t)$. In a RC plate submitted to any loading originating tension stress in at least the first principal direction, cracking onset occurs when the stress reaches the concrete tensile strength:

$$F_{cr}(\boldsymbol{\sigma}^c) = \sigma_1^c - f_{ct} \leq 0 \quad (2.11)$$

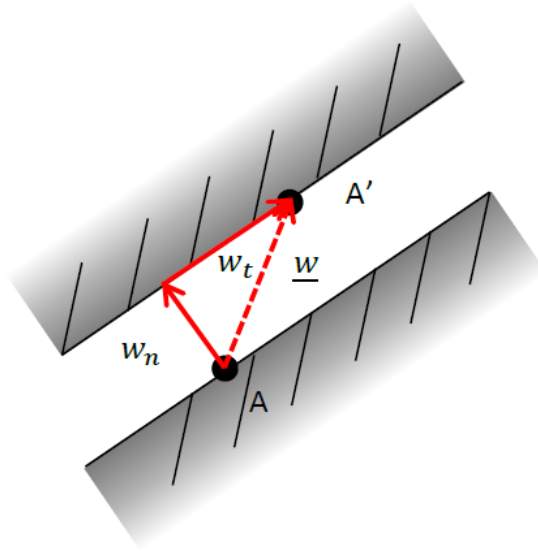


Figure 2.2: Displacement discontinuity at cracks.

The crack pattern evolves with the increasing load until reaching a stabilized crack pattern. If the applied load is cyclic two different families of cracks can be distinguished, characterized by the average crack orientations θ_{r1} and θ_{r2} and spacings s_{r1} and s_{r2} , see Figure 2.3. In order to limit the model to a maximum of two crack families, it is assumed that their orientations are separated at least by 60° .

$$|\theta_{r1} - \theta_{r2}| > \pi/3 \quad (2.12)$$

When a crack family appears following Equation (2.2.2), the crack orientation is fixed as the orthogonal direction to the first principal stress direction. Moreover, the average crack spacing is calculated from the crack orientation with the expression that was first given by Vecchio and Collins (1986):

$$s_r = \left(\frac{\sin |\theta_r|}{s_{rx}} + \frac{\cos \theta_r}{s_{ry}} \right)^{-1} \quad (2.13)$$

where s_{rx} and s_{ry} are the theoretical average crack spacings in the equivalent RC tie-beams in the x and y directions.

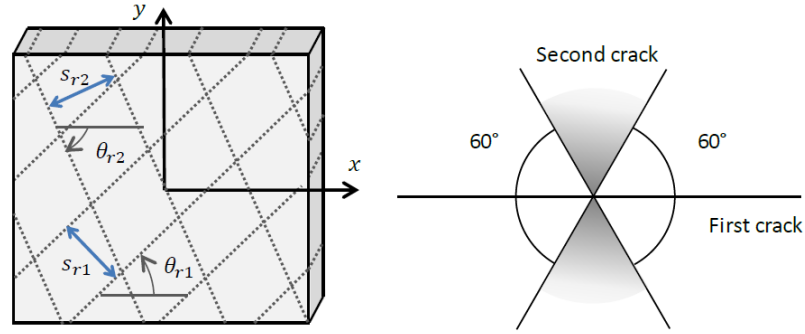


Figure 2.3: Second crack in a RC panel: cracked RC panel geometry and relative orientation between the two cracks.

A crack displacement w originates a number of phenomena which create concrete stresses in the crack surface. The most analysed are:

- *Bridging stress*: normal stress with respect to the crack depending on the normal crack opening w_n , which governs the post-peak concrete tensile behaviour
- *Aggregate interlock*: tangential stresses caused by the resistance that concrete cracks show when a tangential w_t slip is applied. Crack surface is rough because of concrete aggregates which are not cracked since their tensile strength is higher than f_{ct} .
- *Dilatancy stress*: concrete normal stress at crack due to the tangential displacement w_t .
- *Dowel action*: resistance of steel bars to deform transversally to their axis, and therefore opposing to the crack tangential displacement.

The first two will be analysed in the following paragraphs.

Normal crack opening: bridging stress

Bridging stress allow to describe the relation between the normal concrete stress at cracks g_n and the crack opening w_n with the following remarks

- The envelope curve $G_n(w_n)$ is equal to the fracture energy dissipated:

$$\int_0^{+\infty} G_n(w_n) dw_n = G_f \quad (2.14)$$

- Unloading is done elastically (constant crack opening) until compressive stresses are reached. Under compressive stress, crack recloses until a reclosing value which is a fraction of the maximum historical crack opening.
- Reloading is first done elastically (constant crack opening) until tensile stresses are reached; at this moment, crack reopens.

In this model, it is considered that:

- The unloading slope corresponding to the reclosing crack phase for compressive stresses is $\alpha_u E_c$, where α_u it refers to crack unload slope ratio.
- The crack reclosing value is $\alpha_r w_n^{max}$, where w_n^{max} is the historical maximum crack opening and α_r is the crack reclosing ratio.
- When reloading, the envelope curve is attained at the point corresponding to the unloading onset.

In this model a linear bridging stress law $G_n(w_n)$ is retained:

$$G_n(w_n) = \begin{cases} f_{ct} - \frac{f_{ct}^2}{2G_f} w_n & \text{for } 0 \leq w_n \leq \frac{2G_f}{f_{ct}} \\ 0 & \text{for } \frac{2G_f}{f_{ct}} \leq w_n \end{cases} \quad (2.15)$$

That explained above is shown in the Figure 2.4

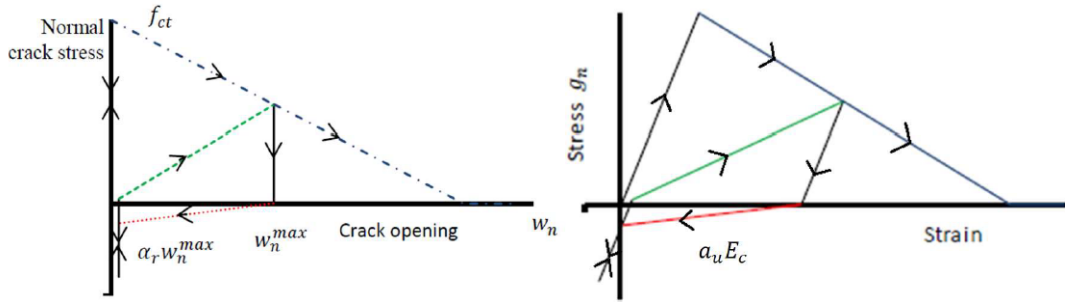


Figure 2.4: Relation between normal concrete stress at cracks g_n and crack opening w_n .

Tangential crack displacement: aggregate interlock

There are several studies in the literature about aggregate interlock;

Walraven [4] propose an analytical study of the aggregate interlock effect in plain concrete considering spherical aggregates that crash with the remaining concrete in the opposite crack surface, Figure 2.5. The analysis considers the frictional forces between aggregate particles and matrix when sliding occurs, and the deformation of the hardened cement matrix.

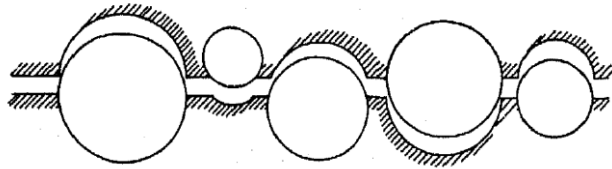


Figure 2.5: Aggregate interlock considered by Walraven.

The Contact density Model of Li et al. [5] (Figure 2.6) adopts the following expression for the aggregate interlock stress τ_{agg} :

$$\tau_{agg} = \tau_{LIM} \frac{(w_t/w_n)^2}{1 + (w_t/w_n)^2} \text{sign}(w_t) \quad (2.16)$$

where τ_{LIM} is the maximum aggregate interlock stress estimated as:

$$\tau_{LIM} = 3.83f_c^{1/3} \quad (2.17)$$

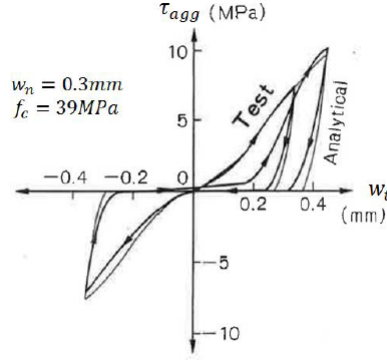


Figure 2.6: Experimental cyclic aggregate interlock test vs. analytical results of Contact Density Model [5].

Similar to the previous one is the model proposed by Gambanova [6] but the peaks of both aggregate interlock and dilatancy stresses are not reached asymptotically but at a limited tangential displacement w_t , Figure 2.7

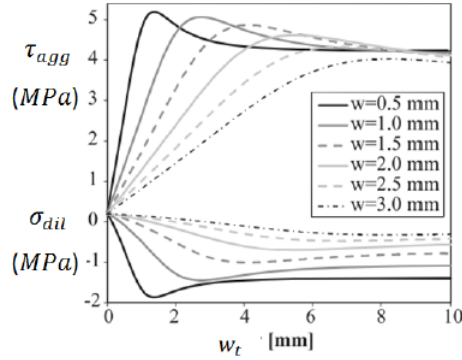


Figure 2.7: Gambanova aggregate interlock law [6].

The definition of the aggregate interlock law in the constitutive model is based on the following observation concerning the aggregate interlock phenomenon just explicated:

- For tangential displacement values in RC structures $w_t \leq 0.5\text{mm}$ the loading stress-tangential displacement curve shown in Figure 2.6 and Figure 2.7 is roughly linear.

- The experimental unloading of Figure 2.6 is done at roughly constant tangential displacement w_t until 0 tangential stress is reached.
- The cyclic response of Figure 2.6 is symmetric in both senses of loading.

Starting from these definitions the obtained tangential stress-tangential displacement w_t curve is shown in Figure 2.8

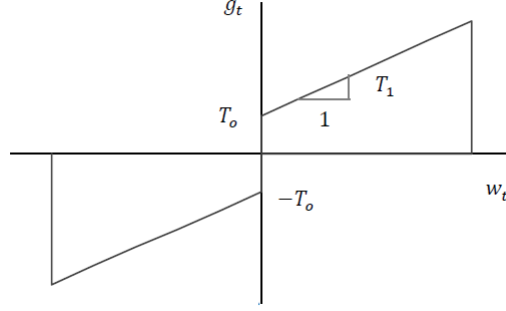


Figure 2.8: Tangential-to crack concrete stress at cracks g_t as a function of the tangential crack displacement w_t .

where T_1 accounts for the aggregate interlock stiffness and T_0 for the initial shear resistance.

2.2.3 Steel-concrete bond-slip

Bond stresses $\underline{\tau} = (\tau_x, \tau_y)$ are transmitted from the x and y reinforcement bars to concrete and they occur when there is a relative slip $\underline{s} = (s_x, s_y)$. It is assumed, the average tension stiffening bond stress $\underline{\tau}^0$ is proportional to the visible and measurable quantity slip at cracks $\underline{v} = (v_x, v_y)$ by means of the global bond stiffness diagonal tensor K^τ :

$$\underline{\tau}^0 = K^\tau \cdot \underline{v} = \sum_{\alpha} K_{\alpha\alpha}^\tau v_{\alpha} \underline{e}_{\alpha} \quad (2.18)$$

The steel-concrete slip at cracks is geometrically related to the crack displacement $\underline{w} = (w_x, w_y)$:

$$v_x = |w_n \sin \theta_r - w_t \cos \theta_r|, v_y = |w_n \cos \theta_r + w_t \sin \theta_r| \quad (2.19)$$

Therefore, the slip \underline{v} is linearly related to the crack displacement \underline{w} by means of the geometrical matrix $M^{vw}(\theta_r)$:

$$\underline{v} = M^{vw}(\theta_r) \cdot \underline{w} \quad (2.20)$$

where the following definition for the matrix $M^{vw}(\theta_r)$, graphically shown in Figure 2.9, is retained:

$$M^{vw}(\theta_r) = \begin{pmatrix} |\sin \theta_r| & -\cos \theta_r \text{sign}(\theta_r) \\ \cos \theta_r & \sin \theta_r \end{pmatrix} \quad (2.21)$$

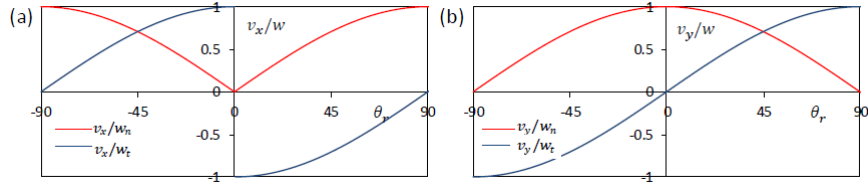


Figure 2.9: Transformation from crack openings to steel-concrete slip in (a) x direction and (b) y direction.

Moreover, in the formulation of the global constitutive model the bond-slip stress appears under the form of an average tension stiffening effect (Figure 2.10). These phenomenon is considered in the law through a "tension stiffening" coefficient k_t .

For further details on the values of these latter coefficients see Appendix A.

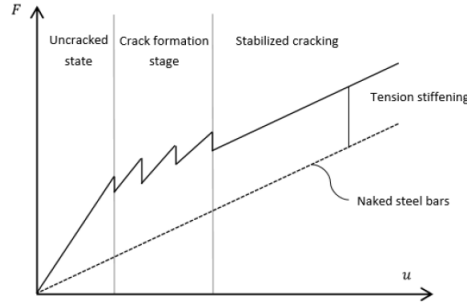


Figure 2.10: Typical force-displacement curve for a RC beam with a displacement-controlled test.

2.2.4 Yielding of steel reinforcement bars

The steel reinforcement bars are supposed to be a one-dimensional medium and to carry only longitudinal forces. Their behaviour is modelled using an elastic - plastic constitutive law:

$$\sigma^{s\alpha} = E_s (\varepsilon_{\alpha\alpha}^{s\alpha} - \varepsilon_{\alpha\alpha}^{ps}) \underline{e}_{\alpha} \otimes \underline{e}_{\alpha} \quad (2.22)$$

where:

- \otimes : Tensor dyadic product
- $\sigma^{s\alpha}$: Membrane stress tensor
- E_s : Steel Young's modulus
- $\varepsilon_{\alpha\alpha}^{s\alpha}, \varepsilon_{\alpha\alpha}^{ps}$: Total and plastic longitudinal strain for steel bars in $\alpha = x, y$ direction.

In this model the yielding of steel reinforcement bars is assumed to be located and concentrated at the crack crossing and the variable steel plastic strain $\underline{\varepsilon}^{ps} = (\varepsilon_x^{ps}, \varepsilon_y^{ps})$ is introduced, which regroups the plastic strains at cracks of x and y steel bars.

2.3 Numerical implementation [2]

The numerical implementation of the model has been done in Code_Aster FE software, developed by EDF using the Discrete Kirchhoff Triangle Generalized (DKTG) finite element. The numerical integration of the constitutive model in each Gauss point of the DKTG finite element it was made through the multicriteria return mapping algorithm which will not be elaborated on in this thesis.

2.3.1 DKTG Finite Element

The Discrete Kirchhoff Triangle Generalized (DKTG) finite elements are isoparametric flat shell elements that do not take into account the curvature of the structure. They are adapted to thin slender structures, where the transverse distortion energy can be considered as negligible with respect to the other deformation energies. An unique integration point is considered in the plate thickness, so they are adapted to constitutive models formulated in generalised stresses and strains, adapted to global modelling approaches for RC plates. The three nodes of the DKTG elements, or the four of the DKQG quadrangle variant element of DKTG, have 5 degrees of freedom: the translations and two in-plane rotations. They are isoparametric elements, and the equivalence between the user-defined axes x, y and the reduced axes η, μ , is shown in Figure 2.11.

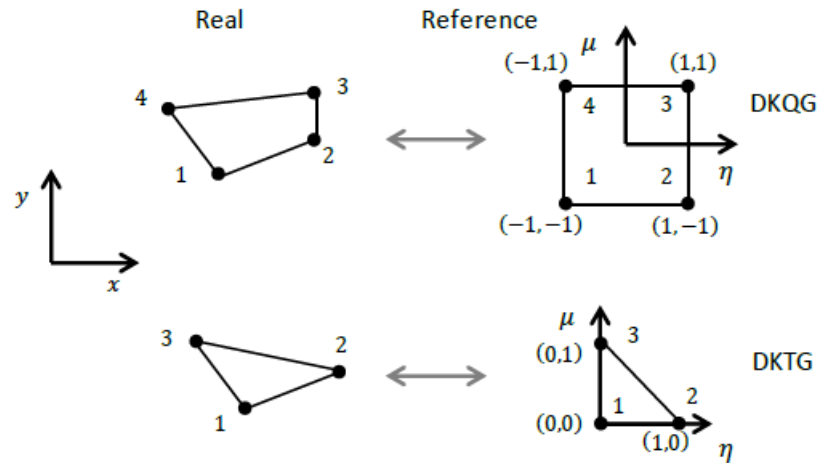


Figure 2.11: Relationship between real and reference DKQG and DKTG elements.

Chapter 3

CEOS.FR

The considered experimental test includes the four walls designed and tested in the framework of the French national research project CEOS.fr (Behaviour and Assessment of Special Structures. Cracking - Shrinkage).

3.1 Experimental test description [7, 8, 9, 10]

Shear-wall specimens were designed and tested in order to analyse shear cracking in thick RC walls under cyclic loading (earthquake). The specimens measure $4.20m$, x $1.05m$, x $0.15m$ and they are equivalent, with a geometrical scale of $1/3$, to the real measures of the wall used in nuclear facilities. Two vertical rebars of $25mm$ and $32mm$ have been added to avoid the cracking due to bending. Furthermore the height/length ratio of $1/4$ ensure a low slenderness of the wall. The redistribution of the shear stresses in the wall is guaranteed by two horizontal thick concrete beams with a high reinforcement ratio connected to its upper and bottom edges. The main characteristics of the specimens are set out in Table 3.1

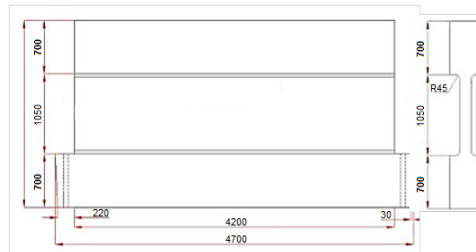


Figure 3.1: Dimensions of the specimen [7]

The specimen is horizontally and vertically connected at the frame only at the edges of the bottom beam. The vertical support being secured by post-stressed bars, in order to avoid uplift for the highest values of the loading assumed for the test. The steel frame, the detail of the section and the reinforcement position are set out in Figure 3.2 and Figure 3.3

The load is applied by two hydraulic jacks placed $100mm$ above the top of the wall by means $300kN$ force increments. The applied loading history was cycling and reversing for wall A, B and D while for wall C the loading history was non-reversing. In the first case three cycles were applied at each force amplitude how can it be seen in Figure 3.4.

	Wall 1	Wall 2	Wall 3	Wall 4
Nature of test	Variation of concrete	Reference	Variation of loading	Variation of reinforcement
Concrete class	C25	C40	C40	C40
Reinforcement	$\Phi 10@100$	$\Phi 10@100$	$\Phi 10@100$	$\Phi 8@80$
Steel ratio / direction	1.05%	1.05%	1.05%	0.84%
Cyclic load history	Reversing	Reversing	Non reversing	Reversing

Table 3.1: Main characteristics of the specimens.



Figure 3.2: Steel frame of the specimen [7]

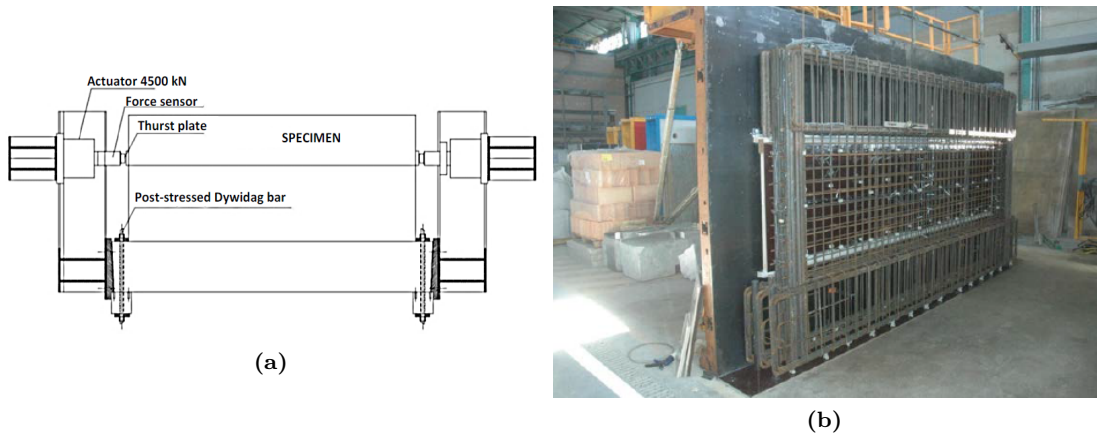


Figure 3.3: Section in the middle of steel frame and of the specimen (a) and reinforcement and part of formwork (b) [7].

To measure the relative displacement between top and bottom massif of specimens, sensors type LVDT were inserted, fixed to a rigid bar hinged on the lower beam and free at the top. Details and arrangement of the sensors are shown in Figure 3.5

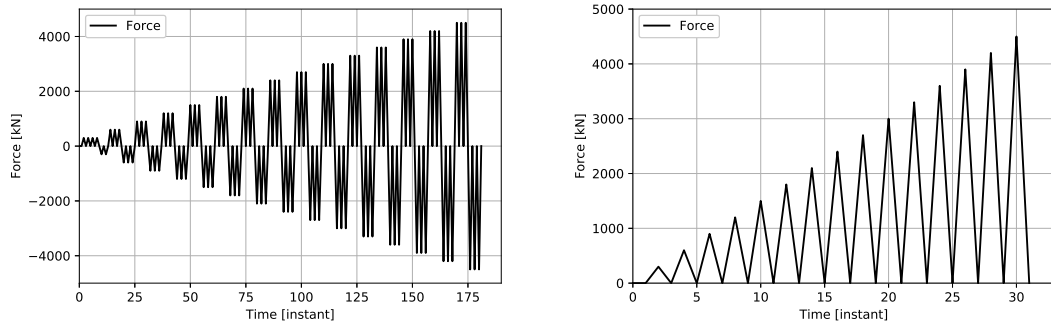


Figure 3.4: Measured load time histories: reversing cycling load (left), non reversing cycling load (right).

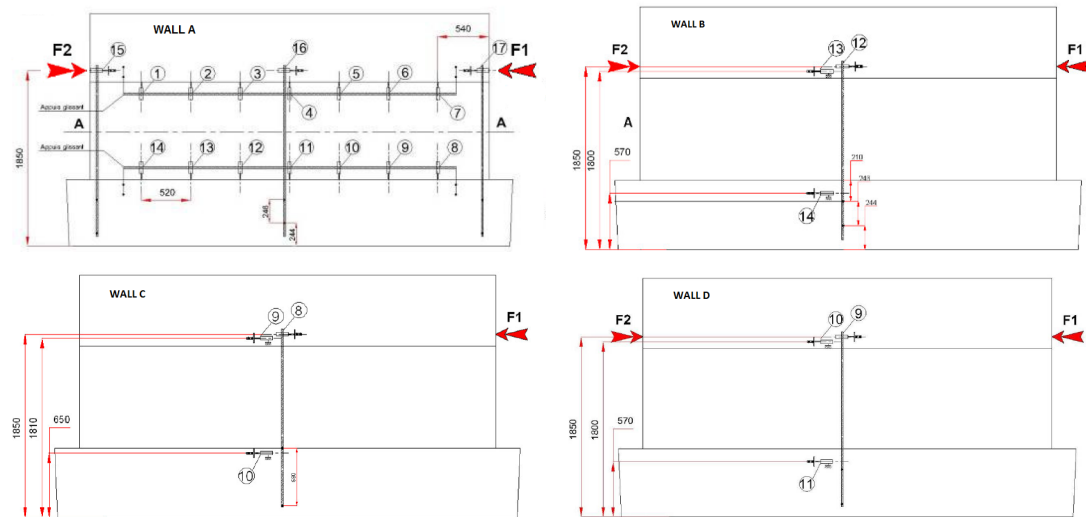


Figure 3.5: Arrangement of sensors for walls A, B, C and D respectively.

3.1.1 Experimental test results [11]

In the next session the main results obtained from the experimental tests will be shown. The global force-displacement curves are defined by the horizontal applied force vs. horizontal relative (between the top and bottom beams) displacement the wall refer to rigid sensors with bar. Figure 3.6 shows the experimental global force displacement curves for the walls. Each cycle causes skew cracking depending on the direction of the applied force; when the force direction is reversed, this set of cracks closes and another family of cracks opens symmetrically with respect to the vertical direction. Crack pattern of walls correspond to a load equal to ± 4200 kN are shown in Figure 3.7. The average inclination angle and spacing between cracks are not significantly affected by the direction of thrust.

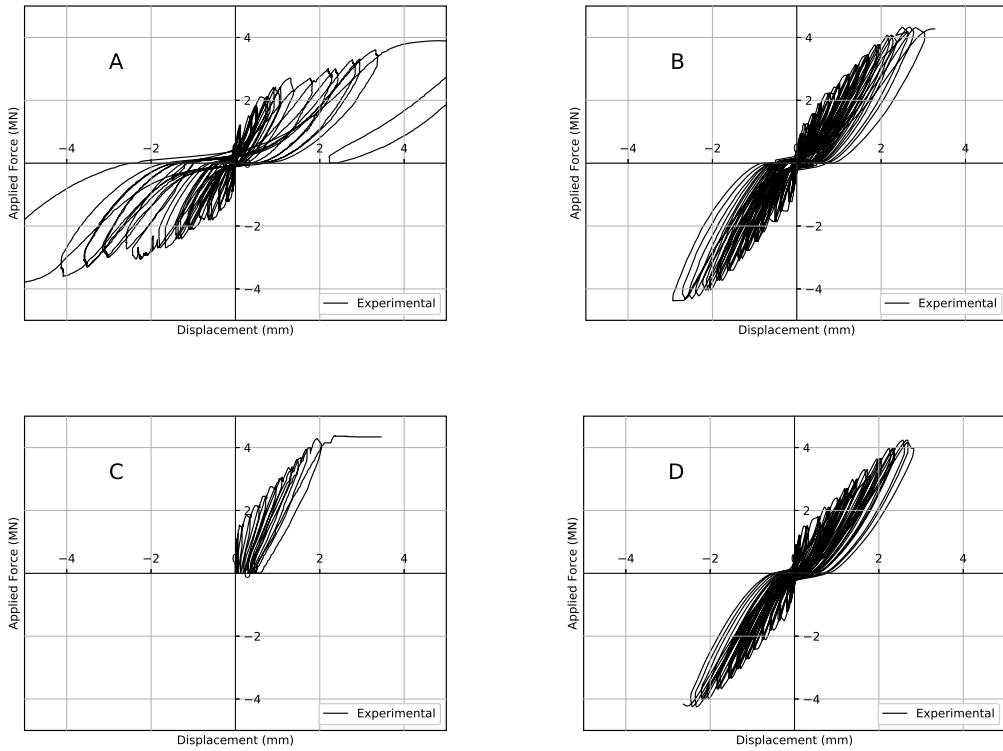


Figure 3.6: Experimental global force-displacement curves.

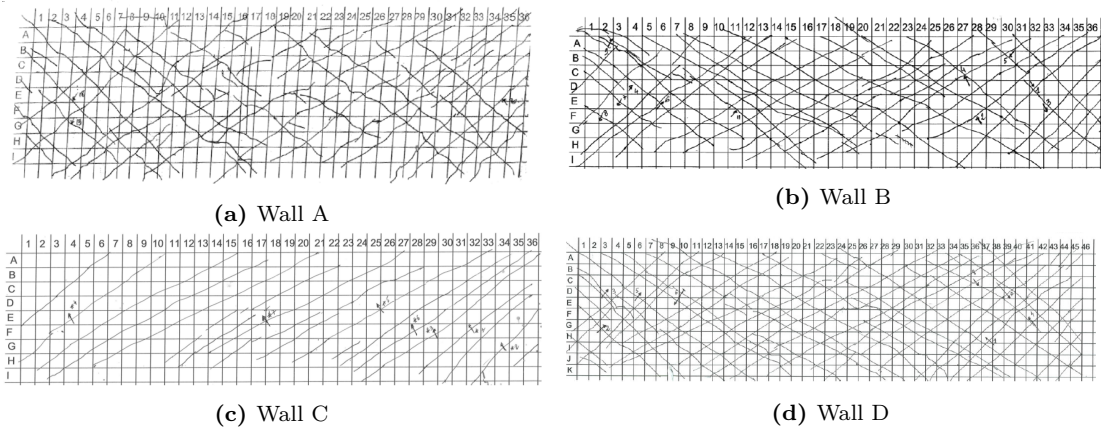


Figure 3.7: Experimental crack orientation.

3.2 Numerical Model

The modelling and the mesh are the same for all walls. The model was already made and was only slightly modified by adding the sensor bar for measuring displacements. The wall and the horizontal thick concrete beams are modelled by plate DKTG plate finite elements in *Code_Aster* FE software while the steel frame is modelled by beam elements. The average pitch of the mesh is about 25 cm. For the calculation of displacements, the rigid bar that supports the LVDT sensors shown in the Figure 3.5 was also modelled (Figure 3.8 (b)).

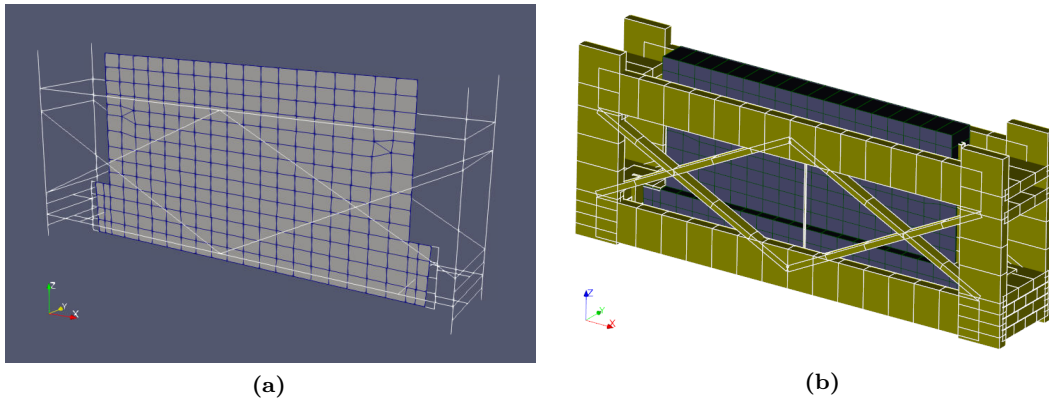


Figure 3.8: FE model of the RC walls (a) and 3D visualization (b).

The test bench is made integral with the reinforced concrete specimen only in the edge of the lower beam. The vertical support being secured by two Dywidag post-stressed bars, in order to avoid uplift for the highest values of the loading assumed for the test. A load of 500 kN is applied on each bar. To ensure instead the horizontal congruence of the displacements there are two metal profiles HEB 700 type. The details of the one just described are visible in the Figure 3.9.

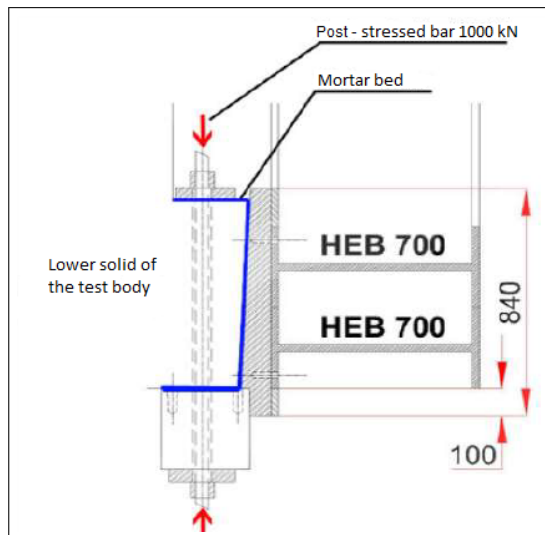


Figure 3.9: Real boundary conditions.

In the numerical model the Dywidag post-stressed bars are modelled by equivalent loads distributed over three nodes (Figure 3.10 (a)). As can be seen in Figure 3.10 (b) the horizontal bond wall-frame is ensured by the rigid discrete elements DIS_T finite elements in *Code_Aster* FE software

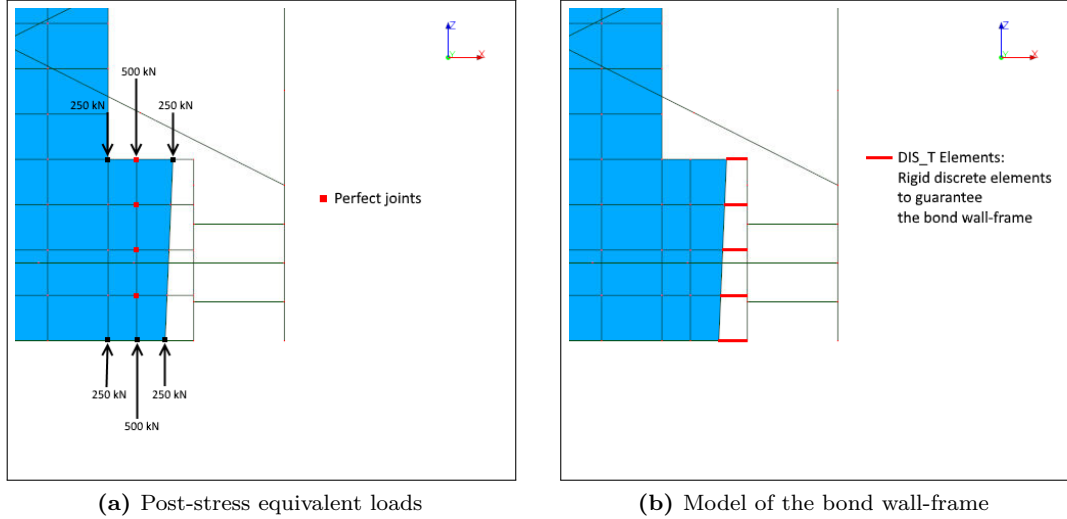


Figure 3.10: Modelled boundary conditions.

3.2.1 Non-linear analysis

Having a low damage the two horizontal thick concrete beams are modelled with an elastic while the CEOS wall has a non-linear behaviour given by the GLRC_HEGIS law. The parameters of GLRC_HEGIS law used are the same in the four walls except for those dependent on the characteristics of concrete or on the amount of the steel reinforcement. Taking into account the problem of the concrete size effect, the experimental values of f_{ct} are reduced by $2/3$. The values of the the fracture energy derive from the experimental tests and they are reduced with the square of the f_{ct} reduction, in order to preserve the post-peak slope of bridging stress curve; Concrete damage is supposed to appear in compression at $\sigma_d = f_c/4$ and the asymptotic damage slope is set to $\gamma_d = 0.3$, so (A.3) gives a damage threshold of k_0 . The theoretical average crack spacings are calculated with (A.2) which differ due to the different cover in each direction. Between cracks, a relatively low tension stiffening effect is supposed to be developed in reason of the cyclic loading: $k_t = 0.2$. The bond-slip stiffness is estimated to $K_l = 10^{11}$ Pa/m. In reason of the cyclic loading and the evolution at the same time of normal w_n and tangential w_t crack displacements, the values of the cyclic bridging stress parameters $\alpha_r = 0.05$, $\alpha_u = 0.05$ are retained. Not being a relevant phenomenon and to avoid convergence problems, the tangential crack opening was not considered and therefore the parameter T_0 is set very large ($T_0 = 100$ MPa), while the parameter T_1 is estimated to 10 GPa/m. Table 3.2 summarizes all the parameters used.

Parameters	Unit	Wall A	Wall B	Wall C	Wall D
ρ_c	[Kg/m ³]	2167	2259	2259	2259
E_c	[GPa]	19.9	27.4	27.4	27.4
ν_c	[-]	0.183	0.13	0.13	0.13
E_s	[GPa]	200	200	200	200
A_{sx}	[cm ² /m]	7.854	7.854	7.854	6.283
A_{sy}	[cm ² /m]	7.854	7.854	7.854	6.283
z	[mm]	55	55	55	55
f_{sy}	[MPa]	555	555	555	555
f_{ct}	[MPa]	1.47	2.37	2.37	2.37
G_f	[J/m ²]	71	80	80	80
α_d	[-]	0.05	0.05	0.05	0.05
α_r	[-]	0.05	0.05	0.05	0.05
k_t	[-]	0.2	0.2	0.2	0.2
T_0	[MPa]	100	100	100	100
T_1	[GPa/m]	10.0	10.0	10.0	10.0
k_0	[Pa]	687	1277	1277	1277
K_l	[Pa/m]	10 ¹¹	10 ¹¹	10 ¹¹	10 ¹¹
γ_d	[-]	0.3	0.3	0.3	0.3
Φ_x	[mm]	10	10	10	8
Φ_y	[mm]	10	10	10	8
s_{rx}	[mm]	124	124	124	124
s_{ry}	[mm]	138	138	138	138

Table 3.2: GLRC_HEGIS parameters for CEOS.fr RC walls.

3.3 Comparison between experimental and numerical results

The experimental loading history of Figure 3.5 is applied on the FE model of the RC walls. Figure 3.11 shows the global force-displacement curves comparison between experimental and the numerical results respectively for the wall A, B, C and D. As can be seen in the figure, both for all the walls, the numerical curve represents the experimental results very well especially in terms of initial stiffness and envelope. For the wall B and D there is a slight underestimation of the residual displacements but overall the law GLRC_HEGIS provides results very close to the experimental ones both in the case of reversible and non-reversible cyclic loading.

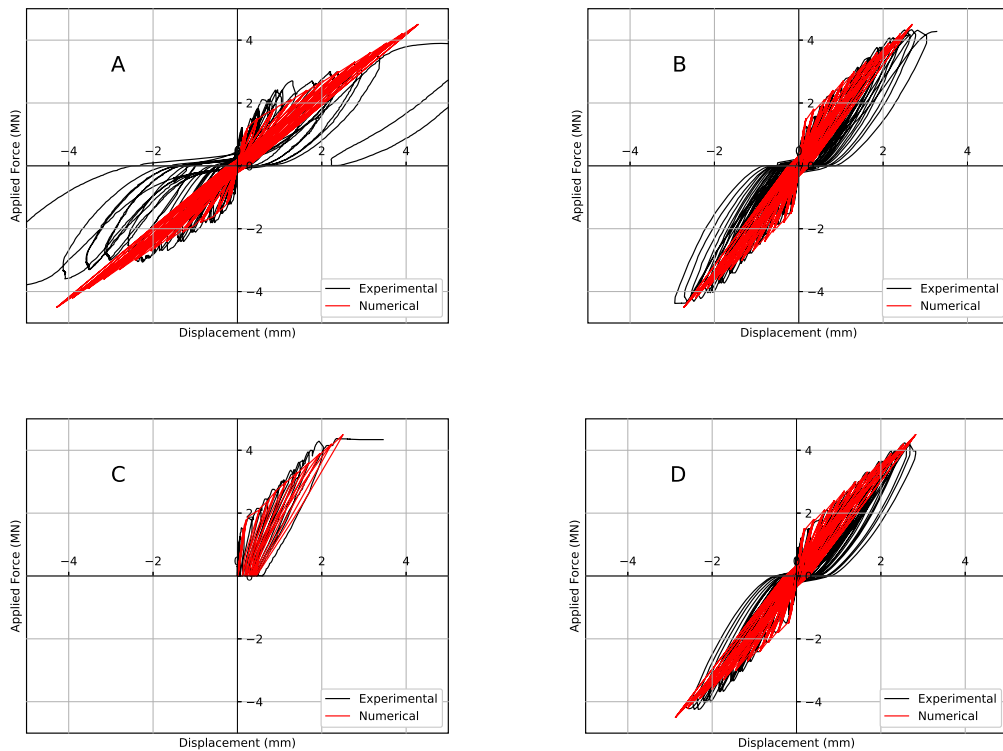
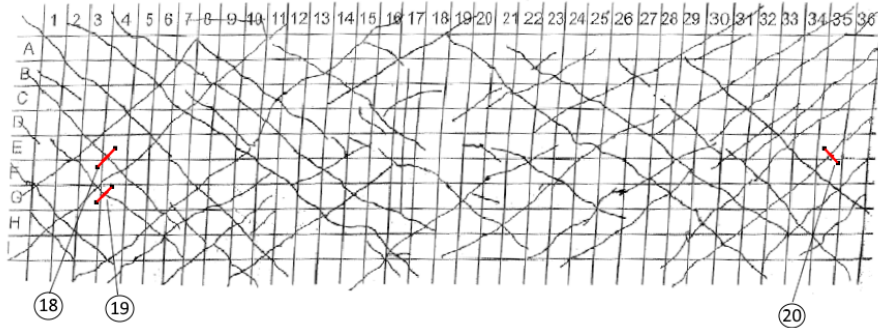


Figure 3.11: Experimental vs. numerical global force-displacement curves.

3.3.1 Crack opening

Figure 3.12, 3.13, 3.14, 3.15 shows the comparison between the experimental and numerical values of crack opening. The sensors arrangement and the comparison between the experimental and the numerical results are shown in the following images.



(a) Sensors arrangement of wall A [7]

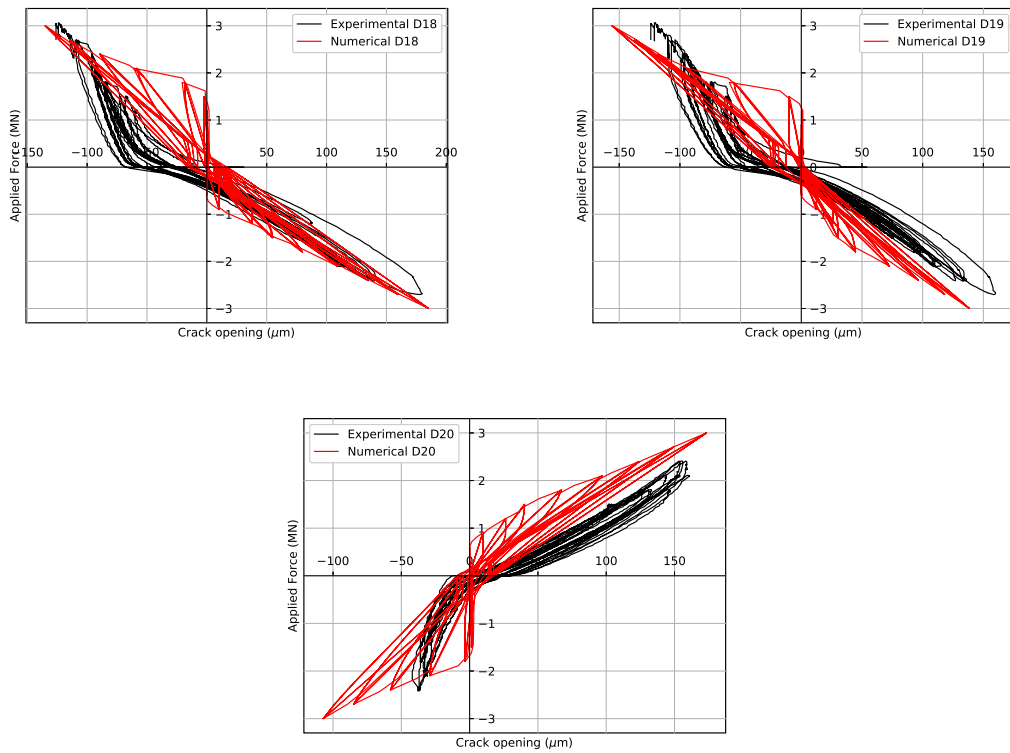
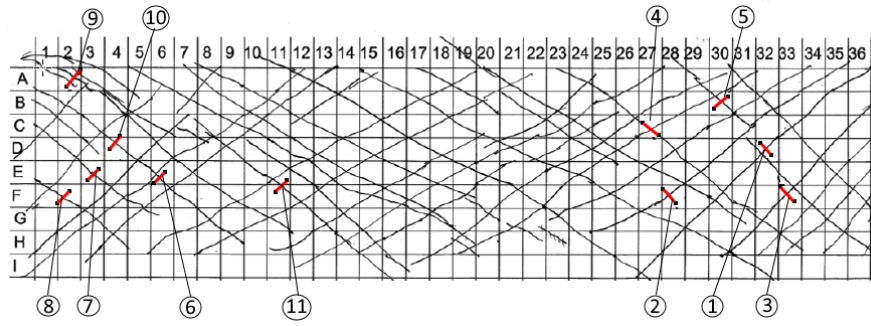
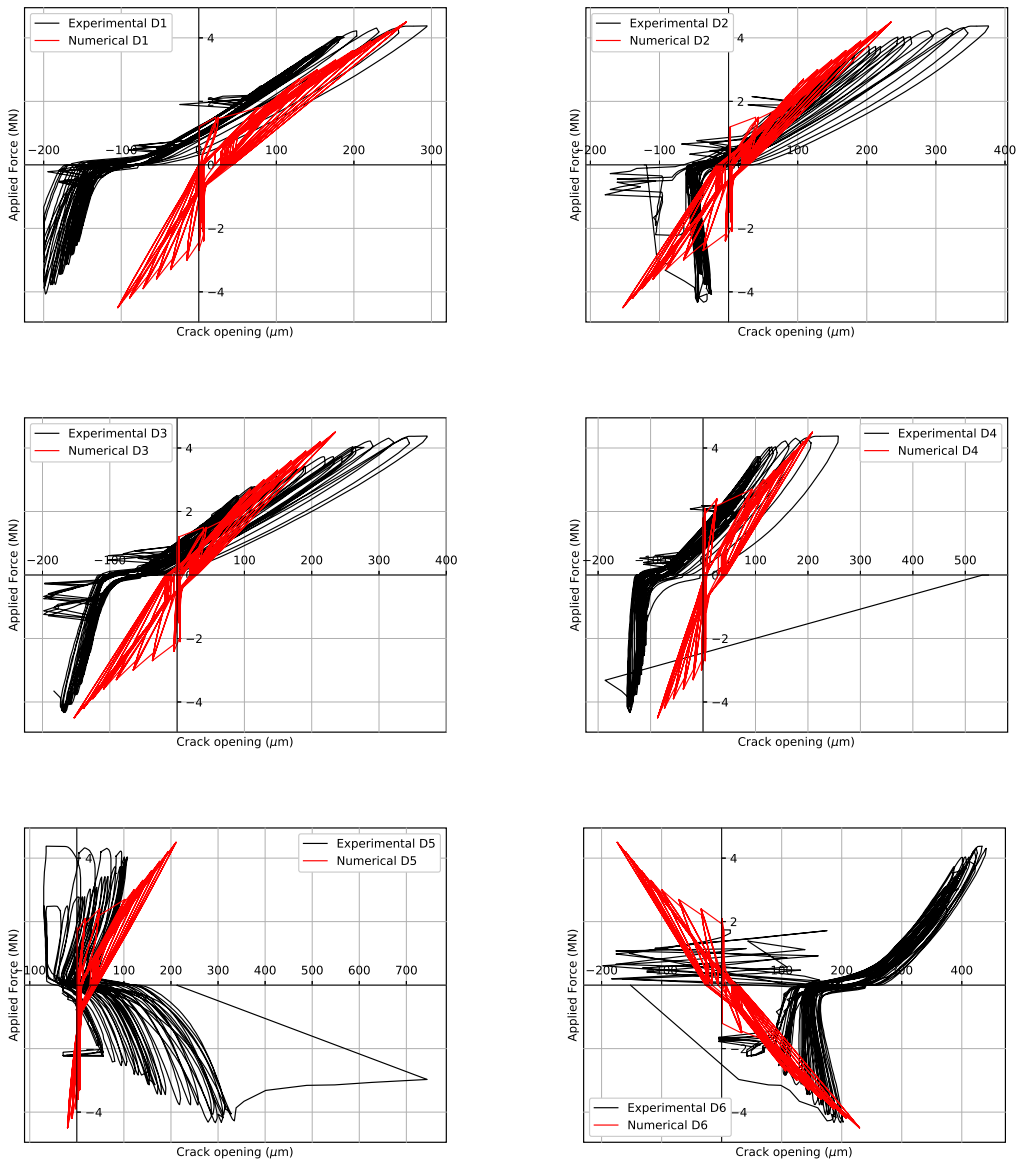


Figure 3.12: Experimental vs. numerical crack opening for wall A at sensors D18, D19 and D20.



(a) Sensors arrangement of wall B [8]



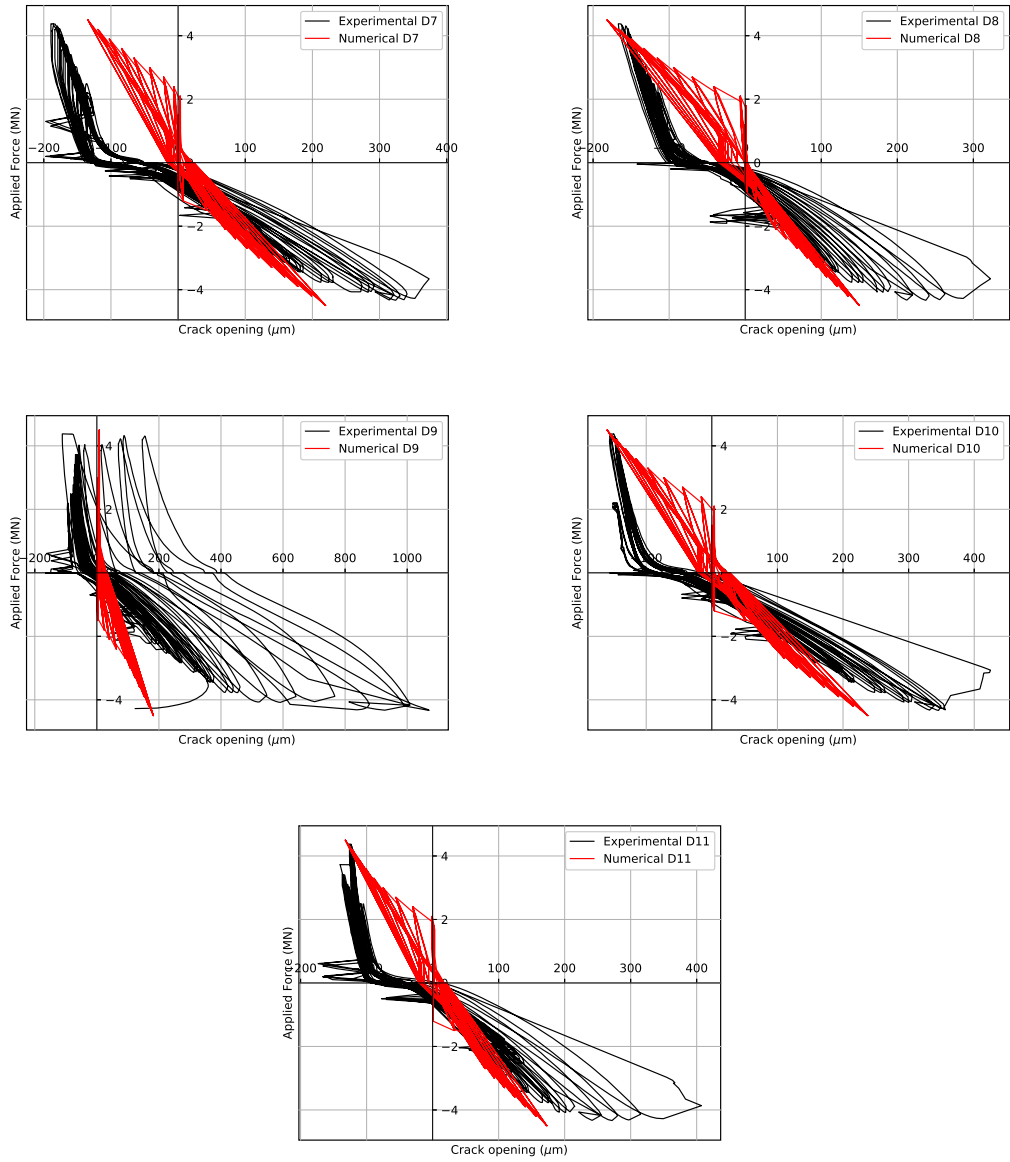
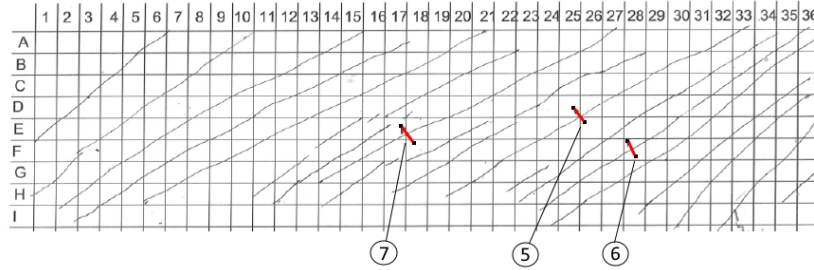


Figure 3.13: Experimental vs. numerical crack opening for wall B at sensors D1 to D11.



(a) Sensors arrangement of wall C [9]

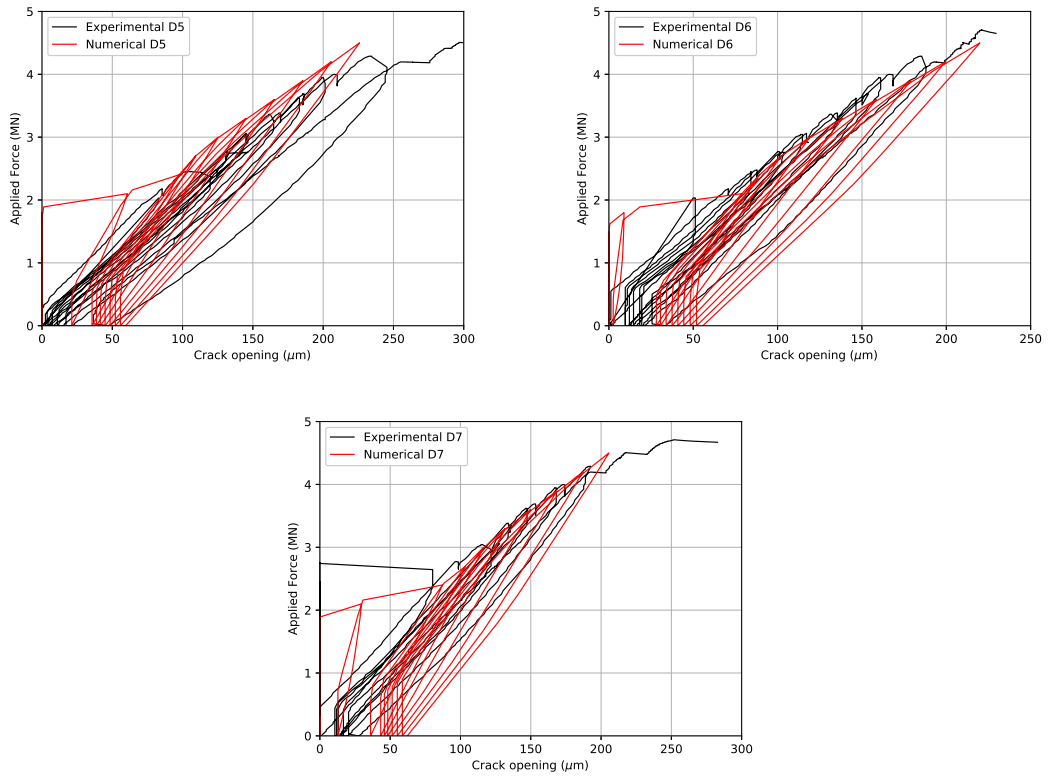
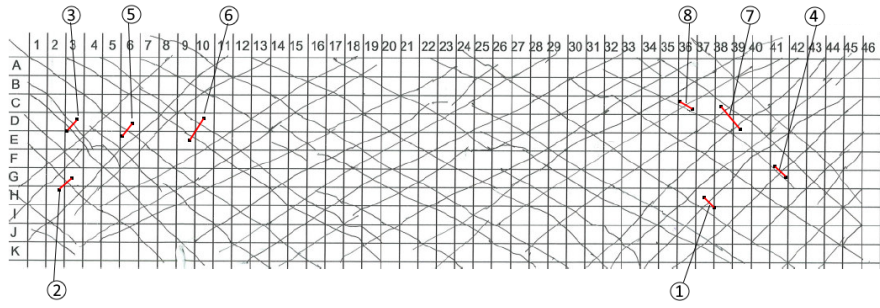
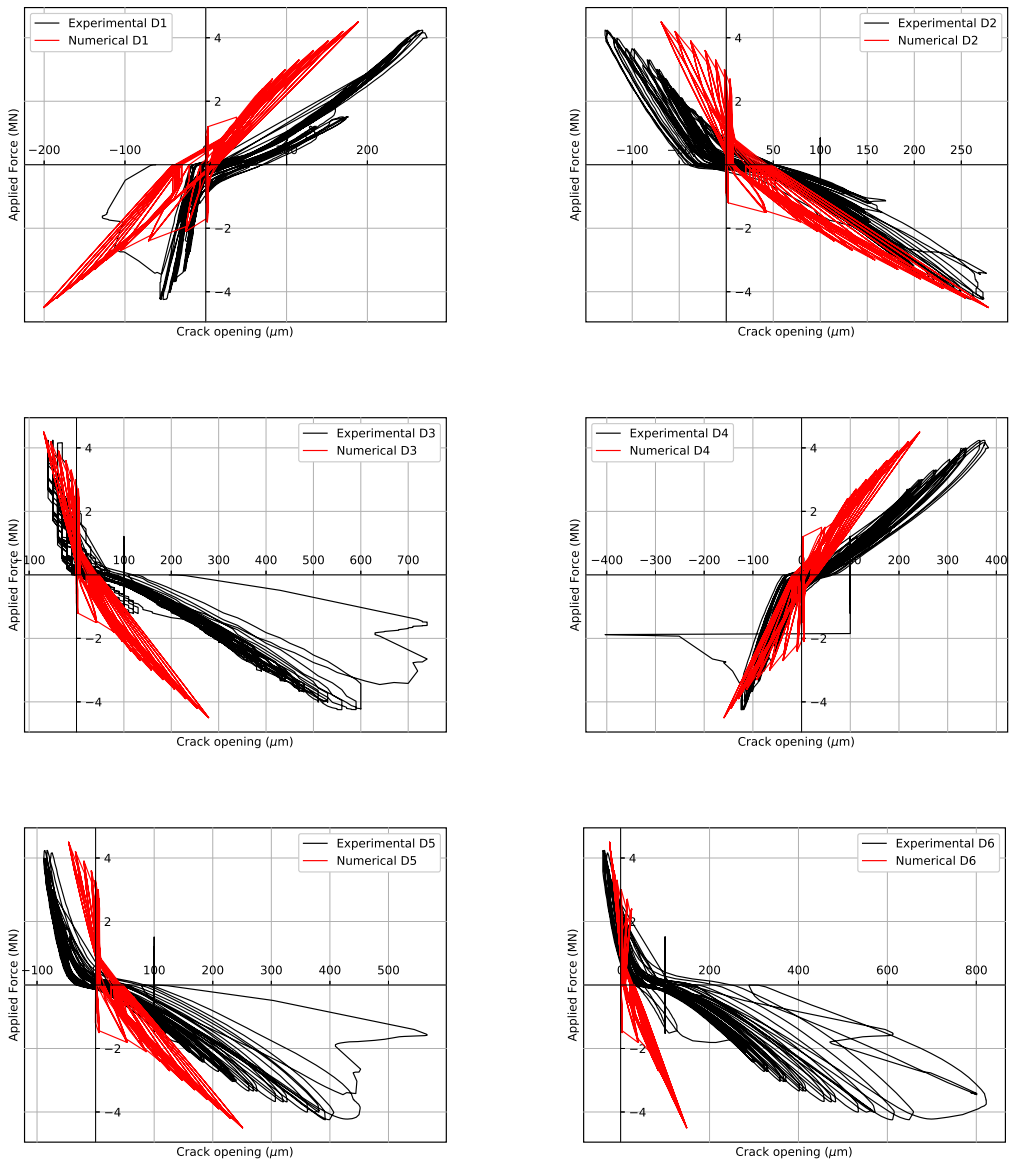


Figure 3.14: Experimental vs. numerical crack opening for wall C at sensors D5, D6 and D7.



(a) Sensors arrangement of wall D [10]



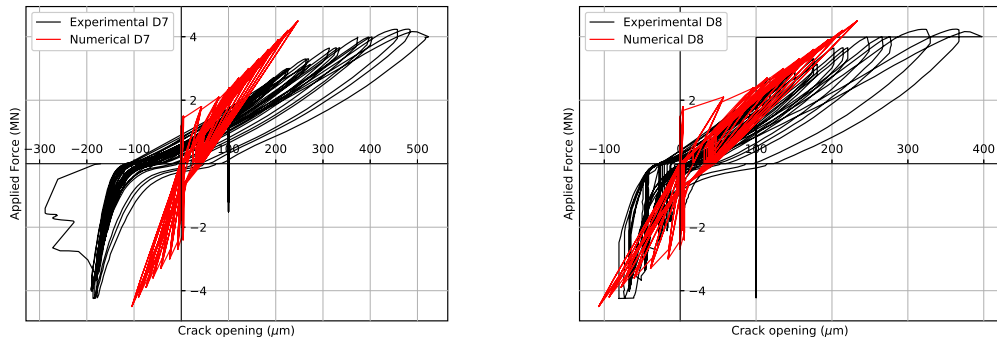


Figure 3.15: Experimental vs. numerical crack opening for wall D at sensors D1 to D8.

Following the results just shown, the subsequent considerations can be made:

- For all sensors there is an imprecision due to the "zero point", value at which the sensors have been installed (just after opening the first crack), which is estimated between 50 and 100 μm .
- In the reversing cyclic load tests, the negative crack opening measured by the sensors represents the compression deformation of the concrete, however the numerical and the experimental values are not comparable.
- As can be seen in Figure 3.11 and in Figure 3.13 some sensors detect two or more cracks and then the two families of curves are not similar and comparable: this is detectable for the sensors D5, D6 and D7 related to wall B and sensors D3, D6 and D7 related to wall D.

3.3.2 Envelope curves

Figure 3.16 shows the experimental and the numerical envelope curves of displacements for all walls. Both experimental and numerical envelope underline that the wall A presents a less stiffness than other walls but it is more ductile in fact it has a greater displacement capacity. This is due to a lower class of concrete. The behaviour of the other walls is quite close as they differ only for the amount of the steel reinforcement. They have less capacity in terms of displacement but reach a greater level of effort.

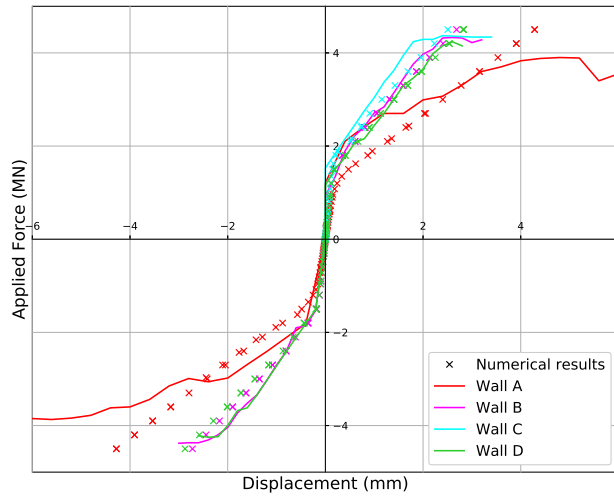


Figure 3.16: Experimental vs. numerical envelope curves.

3.3.3 Crack pattern

Figures from 3.17 to 3.28 show the crack pattern related to wall B for twelve steps of loading. As can be seen, the advancement of the numerical crack opening is very close to the experimental one with a slightly overestimation of the crack spacing. In particular the crack spacing displayed directly in the figures is the $s_{rx,y}$ parameter of the GLRC_HEGIS model calculated through (A.2). To note the presence of the second family of crack due to the inversion of loading. For a better interpretation of the results, the scale relative to the crack opening has not been shown. For an evaluation of the residual crack opening after $F = \pm 4200$ kN refer to the Figure 3.29.

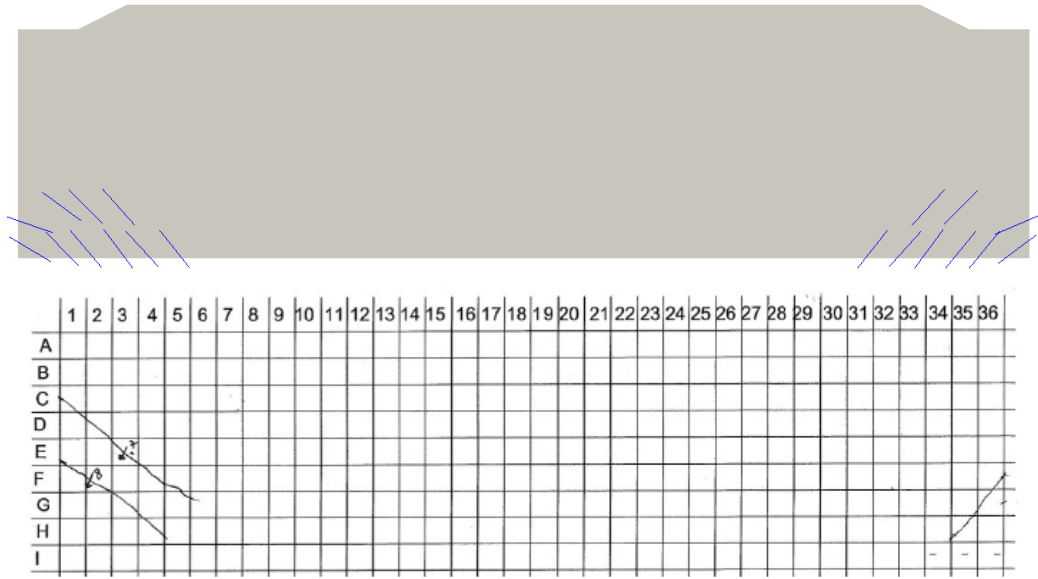


Figure 3.17: Experimental vs. numerical crack pattern at $F = \pm 900$ kN.

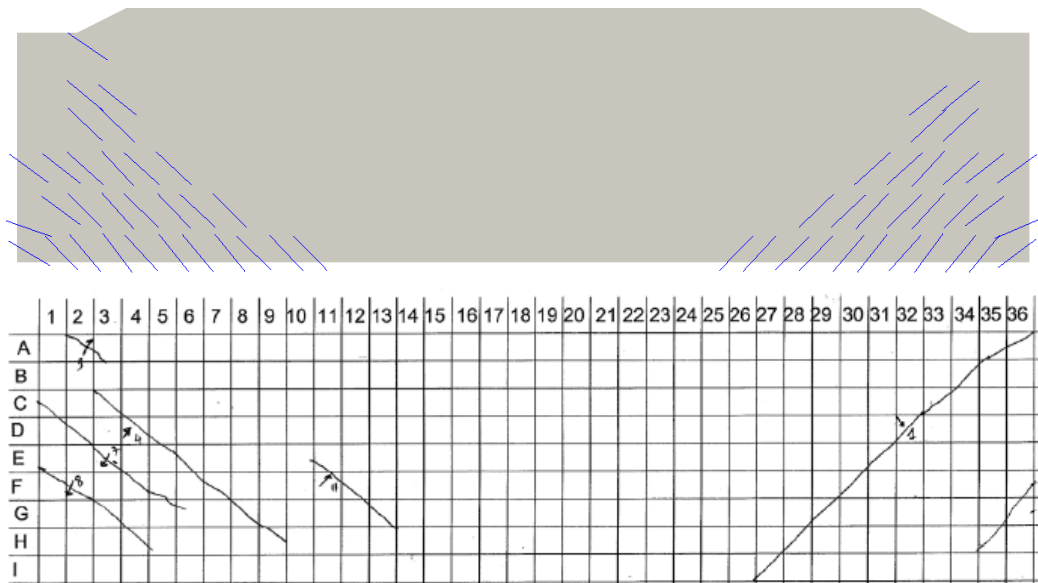


Figure 3.18: Experimental vs. numerical crack pattern at $F = \pm 1200$ kN.

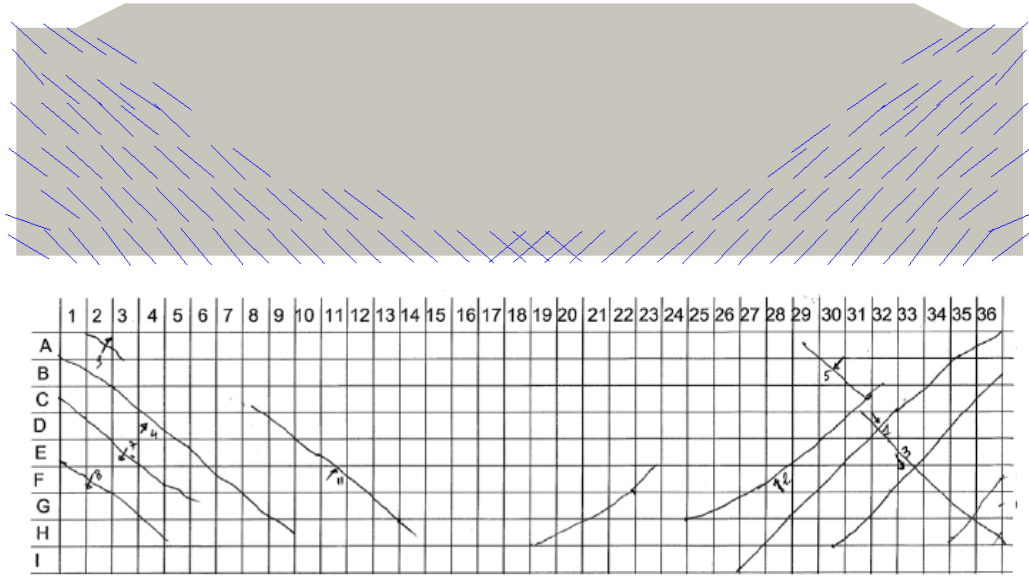


Figure 3.19: Experimental vs. numerical crack pattern at $F = \pm 1500$ kN.

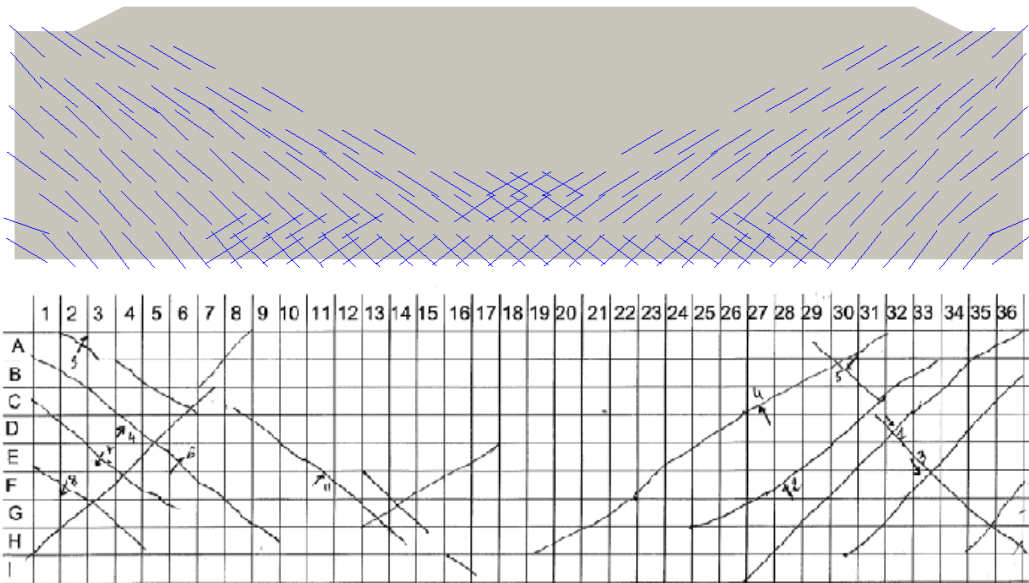


Figure 3.20: Experimental vs. numerical crack pattern at $F = \pm 1800$ kN.

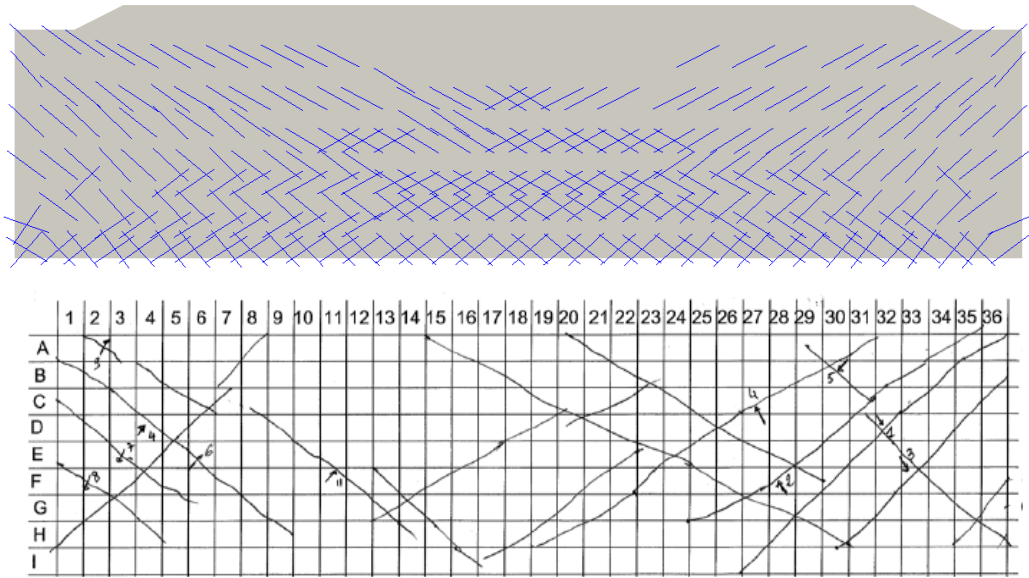


Figure 3.21: Experimental vs. numerical crack pattern at $F = \pm 2100$ kN.

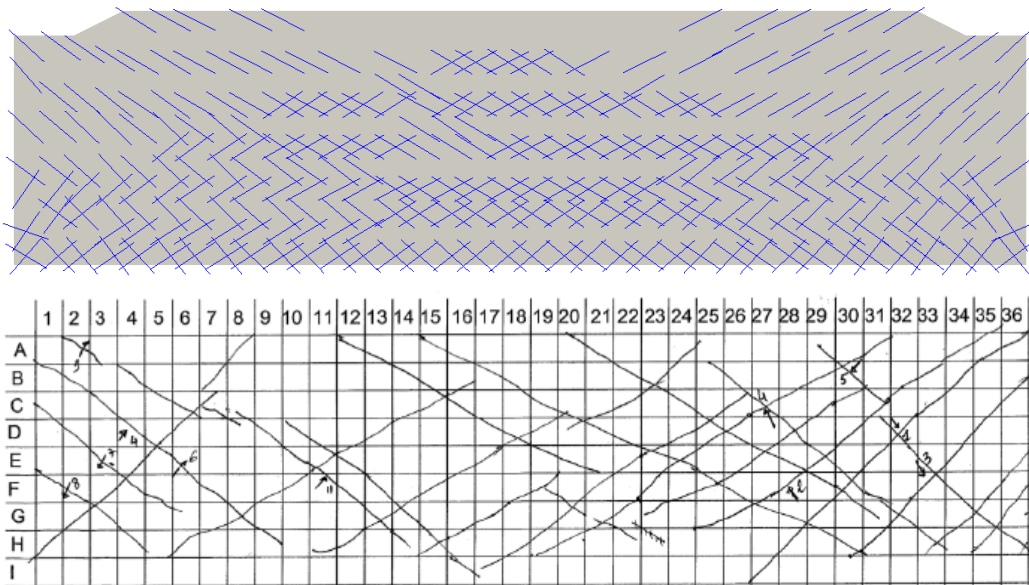


Figure 3.22: Experimental vs. numerical crack pattern at $F = \pm 2400$ kN.

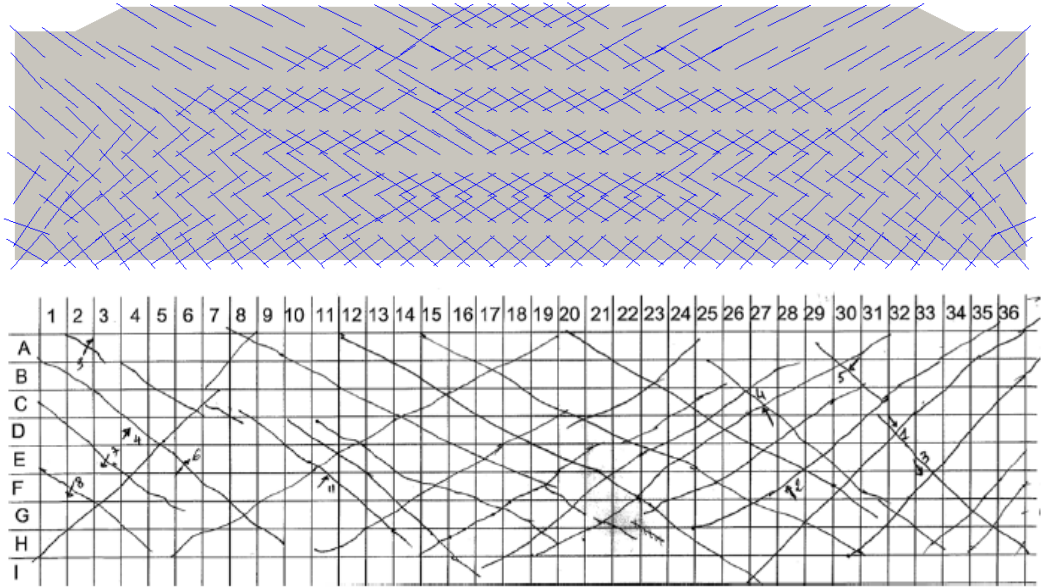


Figure 3.23: Experimental vs. numerical crack pattern at $F = \pm 2700$ kN.

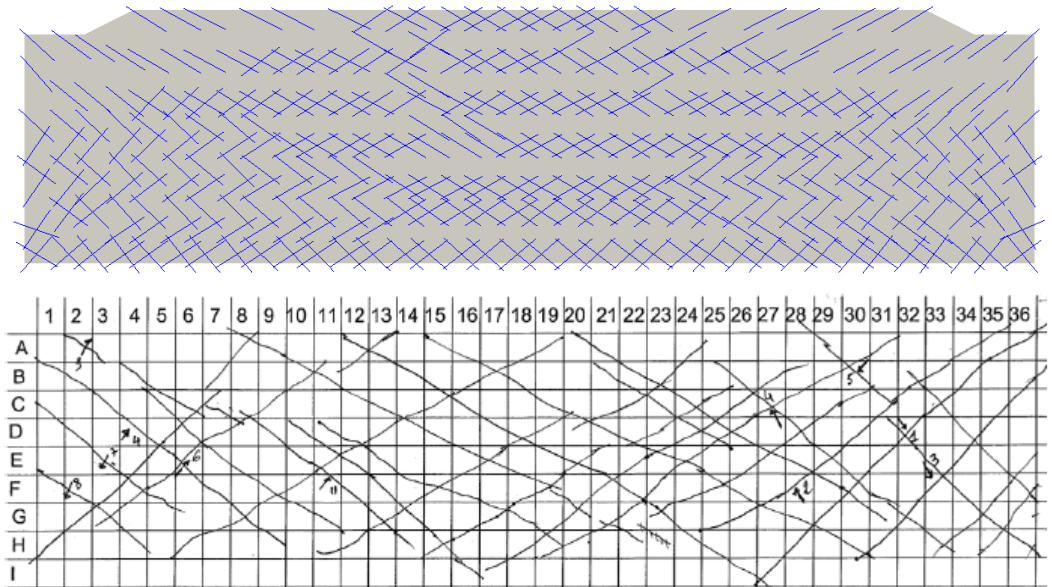


Figure 3.24: Experimental vs. numerical crack pattern at $F = \pm 3000$ kN.

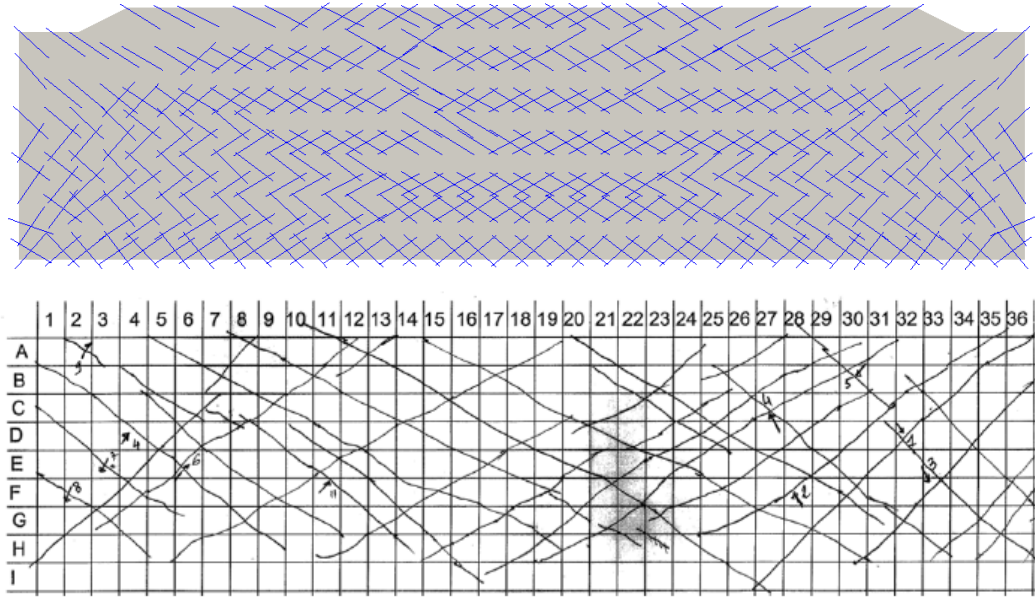


Figure 3.25: Experimental vs. numerical crack pattern at $F = \pm 3300$ kN.

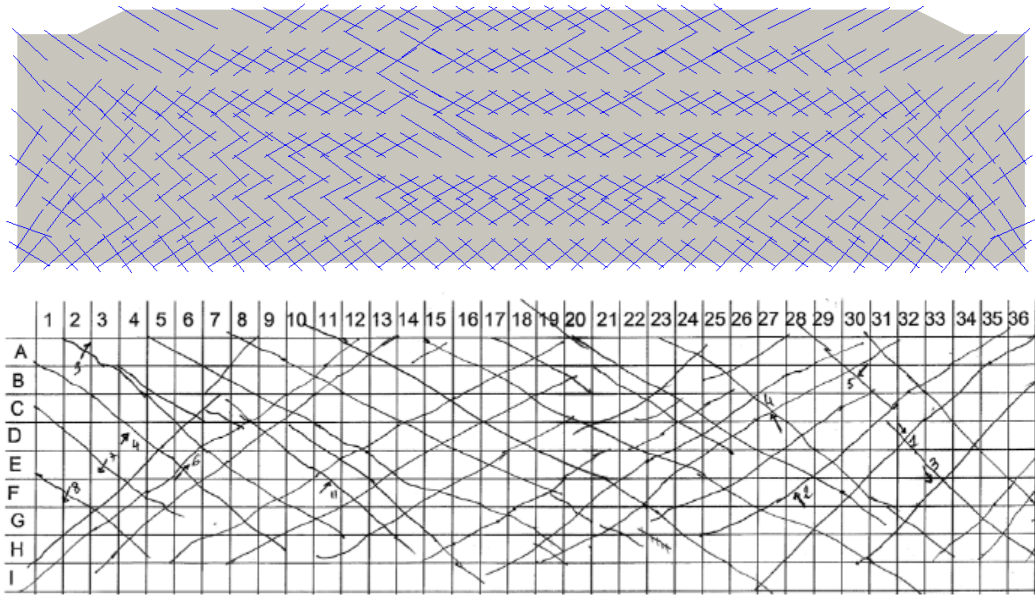


Figure 3.26: Experimental vs. numerical crack pattern at $F = \pm 3600$ kN.

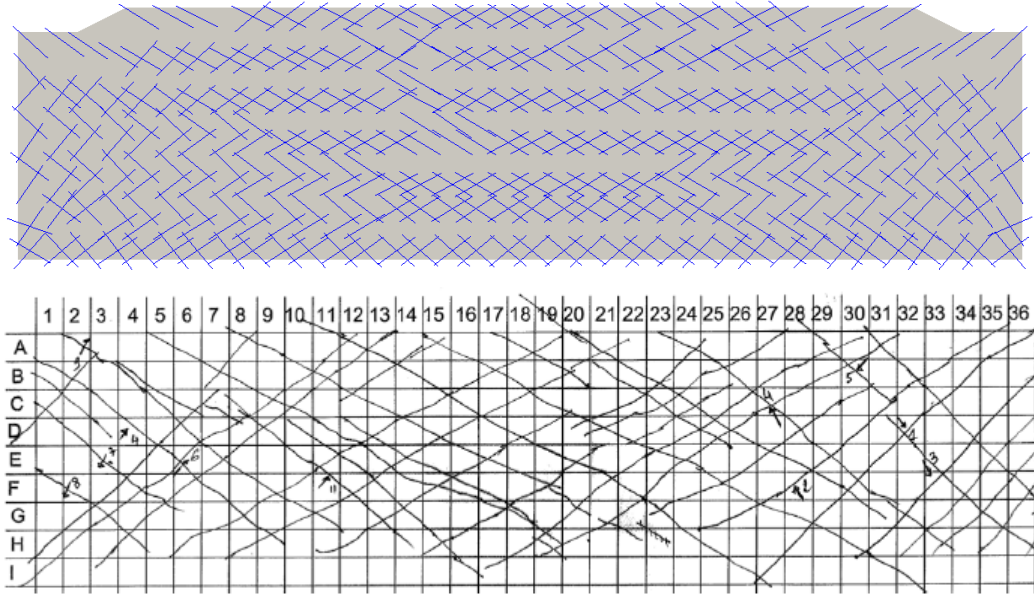


Figure 3.27: Experimental vs. numerical crack pattern at $F = \pm 3900$ kN.

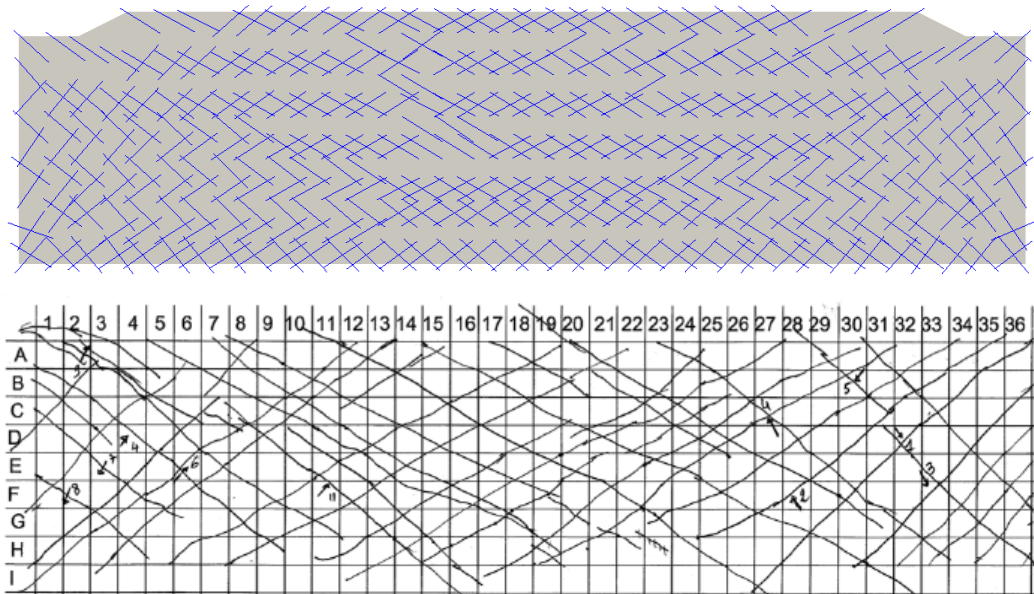


Figure 3.28: Experimental vs. numerical crack pattern at $F = \pm 4200$ kN.

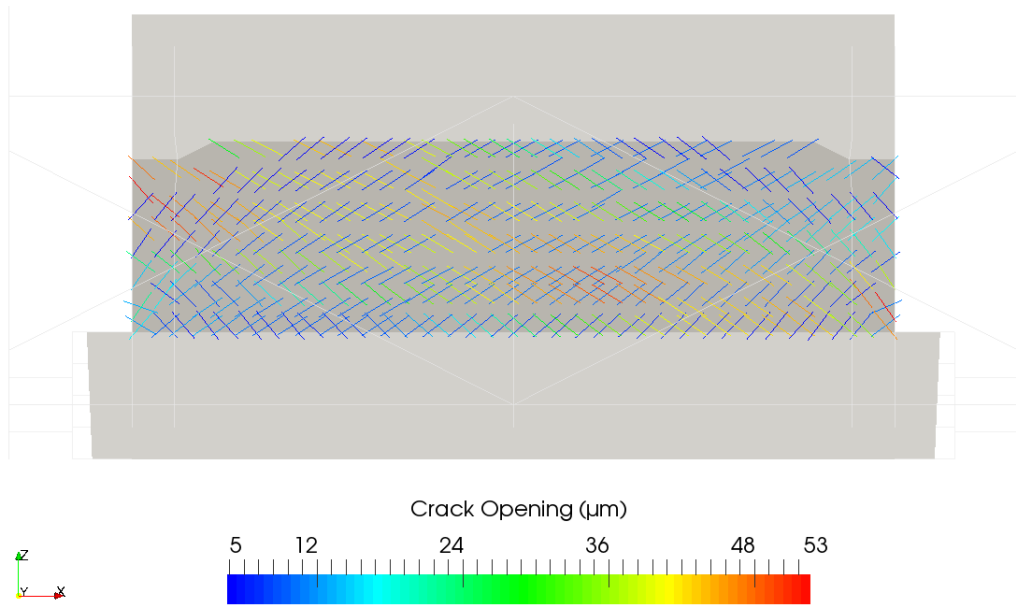


Figure 3.29: Numerical values of the residual cracks after $F = \pm 4200$ kN.

On the basis of the results just obtained and shown, it is possible to make the following considerations:

- For the first load cycles the crack pattern reflects the experimental one very well.
- After the fifth loading step the numerical results go towards a homogenization, in fact from the seventh step it is complicated to extrapolate significant differences in the results.
- In general it is possible to see a slight underestimation of the crack spacing in fact the distance between two experimental cracks is on average about 15/20 cm while in the numerical model a crack spacing value of about 12 cm has been used. The size of the mesh contributes significantly to this underestimation.
- At the penultimate loading step ($F = \pm 4200$ kN) the crack pattern is fully developed and almost homogeneous on the whole wall (Figure 3.29).

Chapter 4

CODE_ASTER TESTS

In this chapter the GLRC_HEGIS model is compared to other global models for RC plates GLRC_DM, DHRC and EIB already implemented in Code_Aster. In particular will be analysed the case of cyclic pure flexion test.

4.1 Cyclic pure flexion test [12]

The global performance is analysed in pure flexion test deepening the results already obtained by Miquel HUGUET-AGUILERA [2] in fact, the same model has been analysed considering at first several load cycles and then an increase of the same over time applied to the relatively high reinforced RC plate of Figure 4.1.

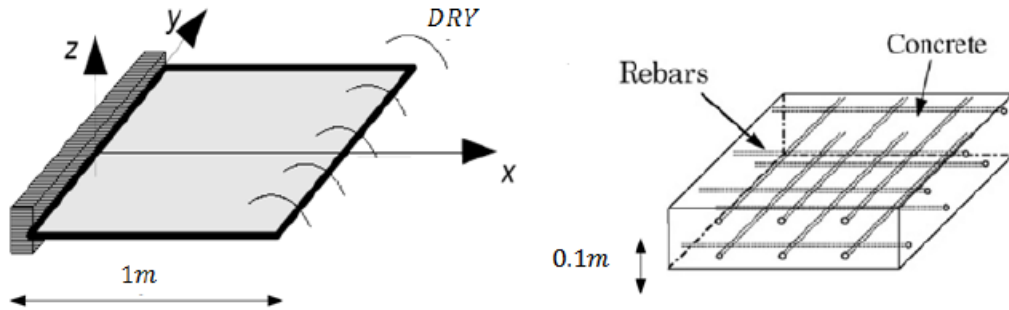


Figure 4.1: Geometry of the considered RC plate.

The dimension of plate are $1m \times 1m$ and $h = 0.1m$. The concrete is characterised by a Young's modulus of $E_c = 32.3Gpa$, a Poisson's ratio of $\nu_c = 0.2$, a tensile strength of $f_{ct} = 3.4Mpa$ and a post-cracking slope equal to 30% of the initial elastic modulus. The plate is reinforced by rebars of $10mm$ spaced by $10cm$ in the top and bottom layers at both x and y direction with a cover of $10mm$. The steel of reinforcement is characterized by a Young's modulus of $E_s = 200Gpa$ and a yielding stress of $f_{sy} = 570Mpa$. The complete set of GLRC_HEGIS parameters is summarised in Table 4.1.

Figure 4.2 shows the FE model of the considered RC plate and the applied boundary conditions.

Parameters	Unit	Value	Parameters	Unit	Value
ρ_c	$[Kg/m^3]$	2500	α_d	$[-]$	0.05
E_c	$[GPa]$	32.3	α_r	$[-]$	0.05
ν_c	$[-]$	0.2	k_t	$[-]$	0.33
E_s	$[GPa]$	200	T_0, T_1	$[MPa], [GPa/m]$	-
A_{sx}	$[cm^2/m]$	7.85	k_0	$[Pa]$	4816
A_{sy}	$[cm^2/m]$	7.85	K_l	$[Pa/m]$	10^{11}
z_{inf}	$[mm]$	35	γ_d	$[-]$	0.3
z_{sup}	$[mm]$	35	Φ_x	$[mm]$	10
f_{sy}	$[MPa]$	570	Φ_y	$[mm]$	10
f_{ct}	$[MPa]$	3.4	s_{rx}	$[mm]$	160
G_f	$[J/m^2]$	143	s_{ry}	$[mm]$	160

Table 4.1: GLRC_HEGIS parameters for CAS_TEST.

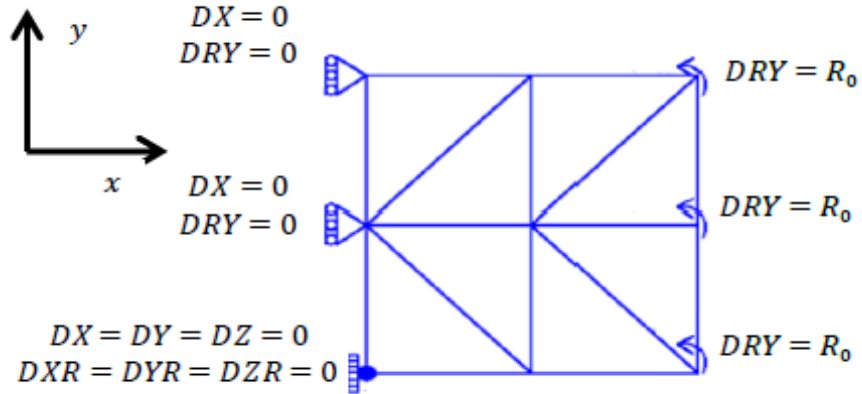


Figure 4.2: FE model and boundary conditions.

4.1.1 Constant rotation over time

The time loading history of Figure 4.3 is applied on the FE model. The imposed constant rotation creates a homogeneous stress state with a cyclical flexion of the lower and upper fibres.

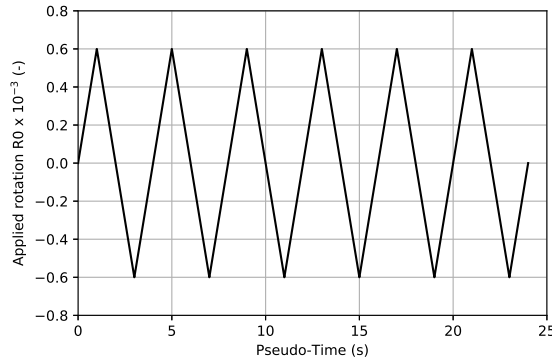


Figure 4.3: Loading history with constant rotation.

By comparing the results of Figure 4.4, the following considerations can be made:

- The elastic stiffness is different because of different model's assumptions.
- Unlike the other laws, GLRC_HEGIS has a bilinear behaviour in the unloading phase. this is due to taking into account in the model the crack re-closure phenomenon.
- The hysteresis surface described by GLRC_HEGIS it's larger than that one described by the other global models.

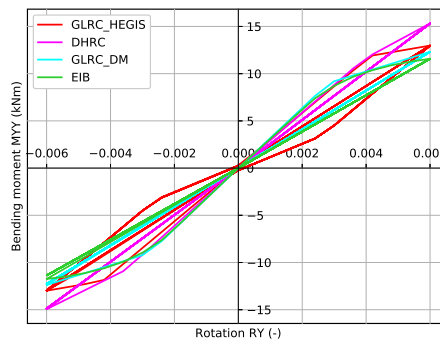


Figure 4.4: Moment-rotation comparison.

As noted previously, taking into account the crack reclosing phenomenon ensures that the energy dissipated by the GLRC_HEGIS model is much larger and above all increasing than that dissipated by the other two global models. In particular for the DHRC and GLRC_DM models the dissipated energy remains constant after the opening of the first and second crack families

(Figure 4.5). Moreover, as can be seen in the Figure 4.6 (b) in this test, energy is only dissipated by crack opening-reclosing mechanism by GLRC_HEGIS model.

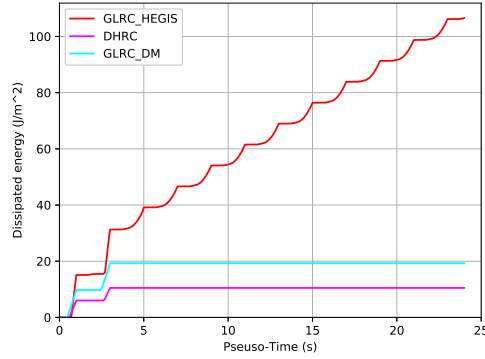


Figure 4.5: Dissipated energy comparison.

The crack opening evolution obtained with GLRC_HEGIS in the top and bottom layers is shown in Figure 4.6 (a). Because of the applied rotation history, it is the bottom layer which cracks firstly, reaching a maximum crack opening of approximately $16\mu m$. When the applied rotation changes its sign, this crack recloses until its residual crack opening while the top layer cracks. Due to the symmetry of the applied load and of the RC plate, the obtained maximum opening of $17\mu m$ in this layer is similar to the previous one, although it is slightly higher because of the previous degradation of the plate. The results obtained in terms of crack opening are exactly identical to those obtained for a single load cycle [2].

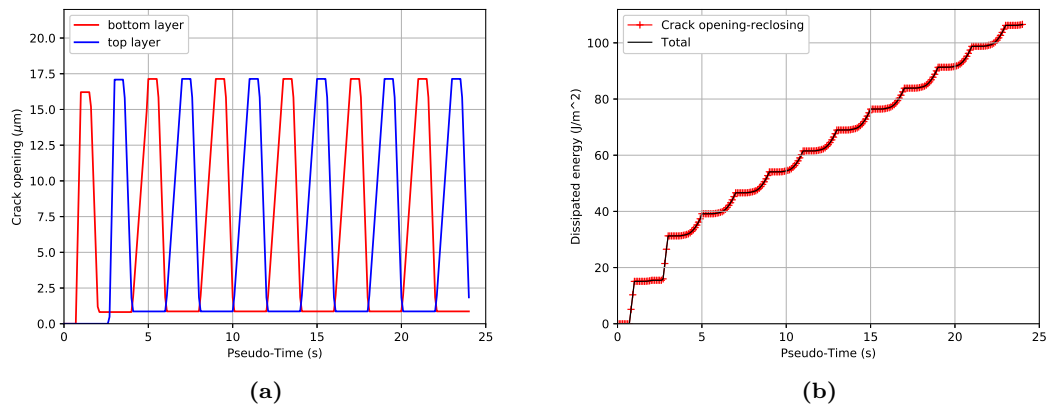


Figure 4.6: GLRC_HEGIS: Crack opening evolution (a) and dissipated energy components.

4.1.2 Incremental rotation over time

In this time loading history (Figure 4.7) the applied rotation is increasing over time. The flexion of the fibres occurs in the same way as the previous load with an increase of the phenomena over time.

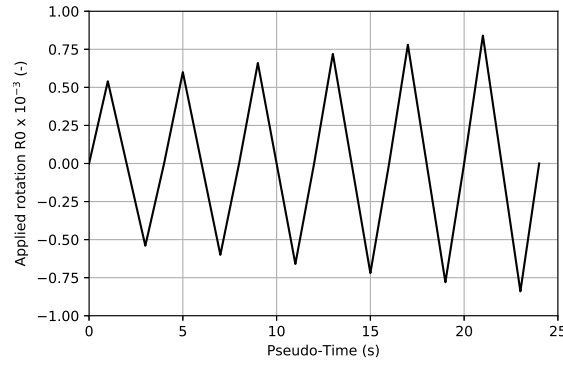


Figure 4.7: Loading history with constant rotation.

As can be seen in the Figure 4.8 the hysteresis surface in this case grows over time due the increase of the crack opening and the residual crack and the same considerations as above can be made. For the same reasons also the energy dissipated for the DHRC and GLRC_DM models grows over time.

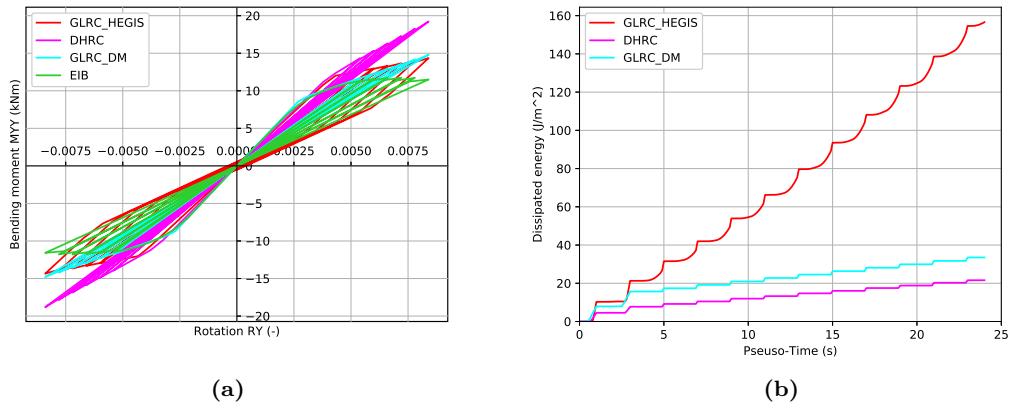


Figure 4.8: GLRC_HEGIS: Moment-rotation (a) and dissipated energy (b) comparison.

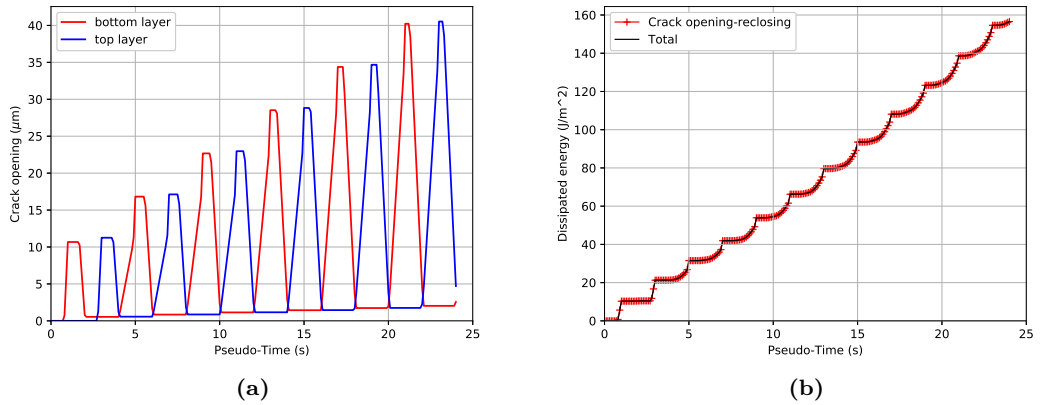


Figure 4.9: GLRC_HEGIS: Crack opening evolution (a) and dissipated energy components (b).

By comparing the results obtained for the two load cases the following considerations can be made:

- The hysteresis surface increases over time for all models due to the damage caused by the increasing applied rotation.
- The energy dissipated by GLRC_HEGIS at the end of load is about 60% larger with the increasing rotation.
- For the increasing load the crack opening is not constant; at the end of load the increase of the crack opening is more than double compared to the previous case; the residual crack also grows over time.
- For both load cases energy is only dissipated by crack opening-reclosing mechanism by GLRC_HEGIS model.

Chapter 5

THREE-POINT BENDING TEST ON RC BEAM

In this chapter will be analysed the behaviour of the GLRC_HEGIS model in the case of out-of-plane pure bending. In particular the numerical model will be compared with the experimental results of a three-point bending test concerning a RC beam.

5.1 Experimental test description

The benchmark [13] consist of a three-point bending test on a RC beam under cyclic loading in order to analyse the global behaviour until the rupture. The beam has a rectangular section of $0.20m \times 0.50m$ and a length of $5.40m$. The distance between the supports is $5.00m$ while the load is applied by an hydraulic jack in the middle of the beam. The main reinforcement consists of two lower bars HA32 and two upper bars HA8. The shear reinforcement consists of stirrups HA8 spaced by $100mm$. Three LVDT sensors are placed one quarter, half and three quarters of the length respectively and they measure global displacements of the beam. Two further comparators are placed at the level of the supports to monitor their movements. The following figures show the test and the beam layout (Figure 5.1 and Figure 5.2).



Figure 5.1: Test layout.

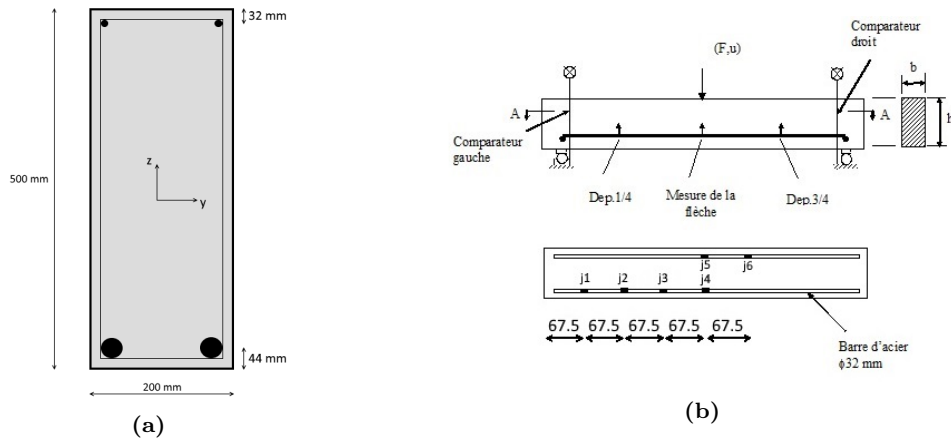


Figure 5.2: Beam's section (a) and sensors arrangement (b).

The principal mechanical characteristics of the concrete and the steel reinforcement are summarized in the following tables:

Material	Class	$E[Gpa]$	$\rho [Kg/m^3]$	$f_c [Mpa]$	$f_{ct} [Mpa]$
Concrete	C35	37.2	2350	36.08	3.68

Table 5.1: Mechanical characteristic of the concrete.

Material	Type	$E[Gpa]$	$\rho [Kg/m^3]$	$f_y [Mpa]$
Steel	500 HA	197.2	7800	466

Table 5.2: Mechanical characteristic of the steel.

The loading is carried out by a hydraulic unit feeding a jack arranged on a cross. The jack used is 1000 kN capacity (+/- 125 mm stroke for an output signal of +/- 10V). Figure 3.17 shows the applied load history of the static cycling load.

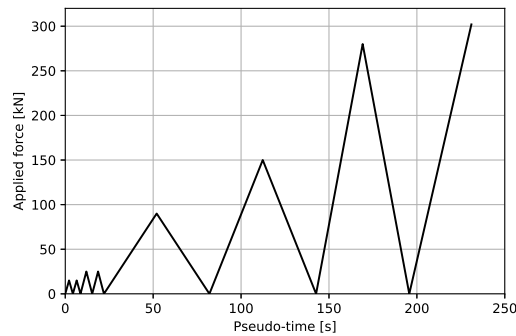


Figure 5.3: Measured load time history.

5.1.1 Experimental test results

The sensors placed at one quarter, half and three quarter of the total length measure the displacements for each of the eight load cycles. After the rupture the deformation control allows the trace the curves also for the post-break stretch. The deformations of the lower reinforcement bars were also measured using sensors J1-J6. The global experimental results of the force-displacement curves and the steel deformation are shown below.

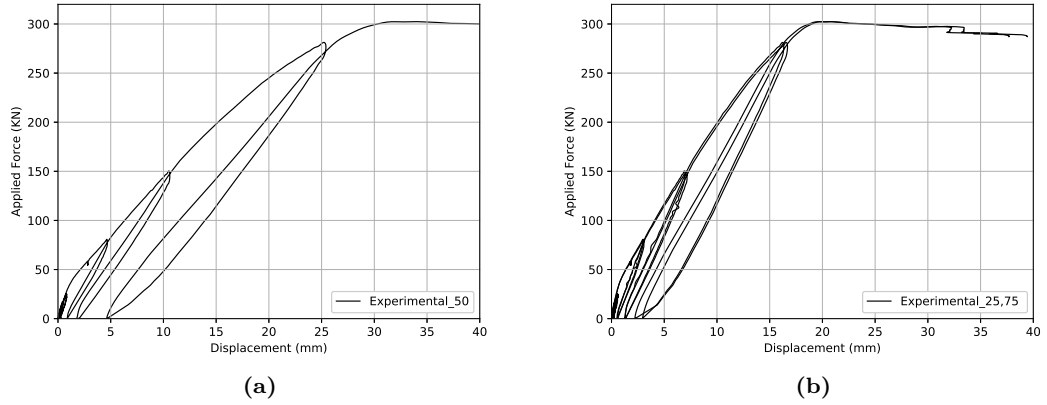


Figure 5.4: Global experimental force-displacement curves at half (a), one quarter and three-fourth of the length (b).

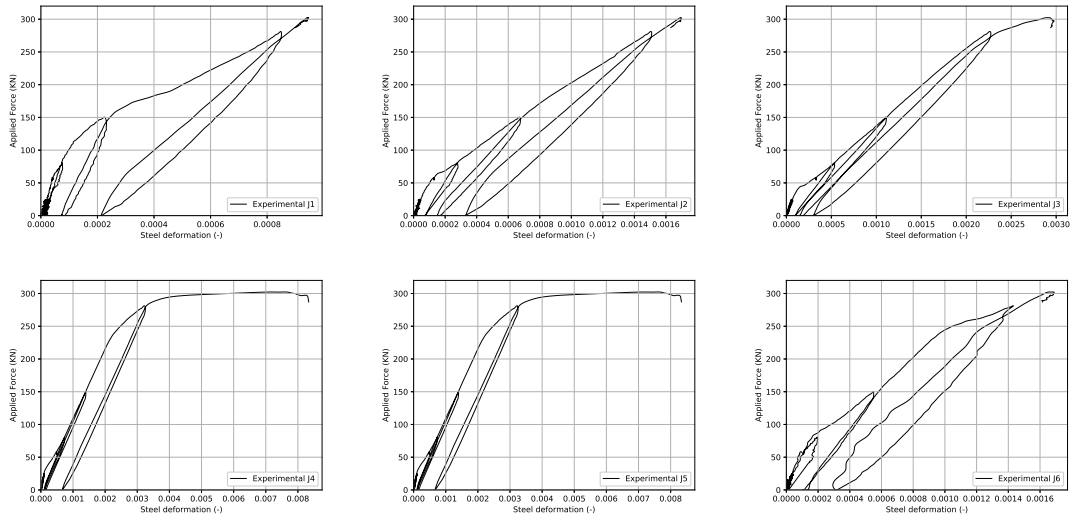


Figure 5.5: Experimental steel deformation given by sensors J1-J6.

5.2 Numerical model

The beam is modelled by plate DKTG plate finite elements in *Code_Aster* FE software. The mesh is composed of 2D quadrangular elements. The boundary conditions simulate the real supports of the beam and a linear distribution of the applied concentrated force was used. The mesh, horizontal with elements equidistant from each other, was used to simulate the case of pure bending. The FE model used for the beam is shown in Figure 5.6.

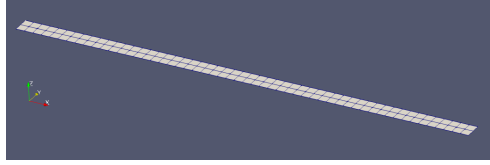


Figure 5.6: FE model of the RC beam.

5.2.1 Non-linear analysis

The beams is modelled with a non-linear behaviour given by GLRC_HEGIS. Taking into account the problem of the concrete size effect, the experimental value of f_{ct} is reduced by $2/3$. The value of the the fracture energy is calculated with (A.1) and it is reduced with the square of the f_{ct} reduction, in order to preserve the theoretical post-peak slope of bridging stress curve. Concrete damage is supposed to appear in compression at $\sigma_d = f_c/6$ and the asymptotic damage slope is set to $\gamma_d = 0.2$, so (A.3) gives a damage threshold of $k_0 = 389$ Pa. The theoretical average crack spacings are calculated with (A.2), obtaining $s_{rx,sup} = 186$ mm, $s_{rx,inf} = 89$ mm and $s_{ry} = 138$ mm. Furthermore, for $s_{rx,inf}$ it was used a value equal to 100 mm obtained from the available images of the crack state; Between cracks, a relatively low tension stiffening effect is supposed to be developed in reason of the cyclic loading: $k_t = 0.2$. The bond-slip stiffness is estimated to $K_l = 10^{11}$ Pa/m. In reason of the cyclic loading and the evolution at the same time of normal w_n and tangential w_t crack displacements, the values of the cyclic bridging stress parameters $\alpha_r = 0.05$, $\alpha_u = 0.05$ are retained. Aggregate interlock parameters are estimated to $T_0 = 0.01$ MPa and $T_1 = 10$ GPa/m. Table 5.3 summarizes all the parameters used.

Parameters	Unit	Value	Parameters	Unit	Value
ρ_c	[Kg/m ³]	2350	α_r	[-]	0.05
E_c	[GPa]	37.2	k_t	[-]	0.2
ν_c	[-]	0.2	T_0	[MPa]	0.01
E_s	[GPa]	195	T_1	[GPa/m]	10
$A_{sx,sup}$	[cm ² /m]	5.03	k_0	[Pa]	389
$A_{sx,inf}$	[cm ² /m]	80.40	K_l	[Pa/m]	10 ¹¹
A_{sy}	[cm ² /m]	5.03	γ_d	[-]	0.2
z_{inf}	[mm]	206	$\Phi_{x,sup}$	[mm]	8
z_{sup}	[mm]	218	$\Phi_{x,inf}$	[mm]	32
f_{sy}	[MPa]	466	Φ_y	[mm]	8
f_{ct}	[MPa]	2.45	$s_{rx,sup}$	[mm]	186
G_f	[J/m ²]	62	$s_{rx,inf}$	[mm]	100
α_d	[-]	0.05	s_{ry}	[mm]	138

Table 5.3: GLRC_HEGIS parameters for RC beam.

5.3 Comparison between experimental and numerical results

The Figures 5.7 and 5.8 show the comparison between the experimental and numerical results obtained with the GLRC_HEGIS model. For the force-displacement curves the loading and unloading phases coincide with a slight underestimation of the residual displacements and a overestimation of the maximal displacement at the peak. It should be emphasized that for the global force-displacement curves the analyses only concerned the loading and unloading phases and were not studied in depth to study post-peak behaviour.

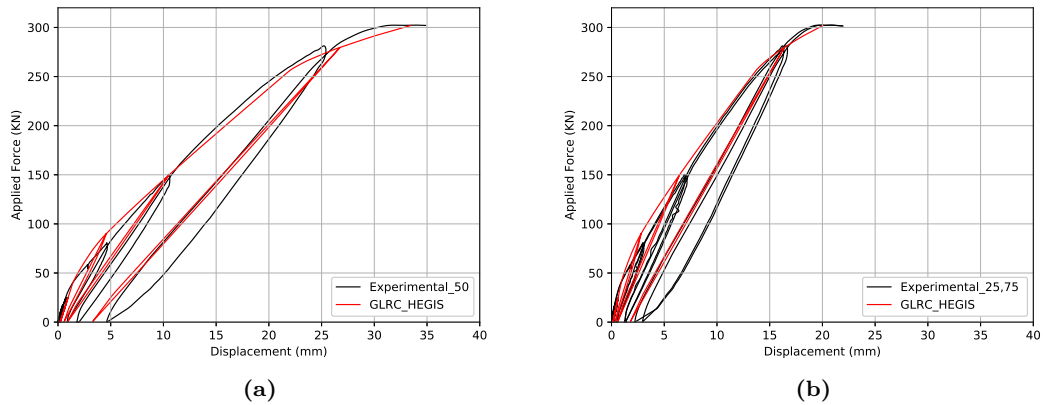


Figure 5.7: Global experimental vs. numerical force-displacement curves at half (a), one quarter and three-fourth of the length (b).

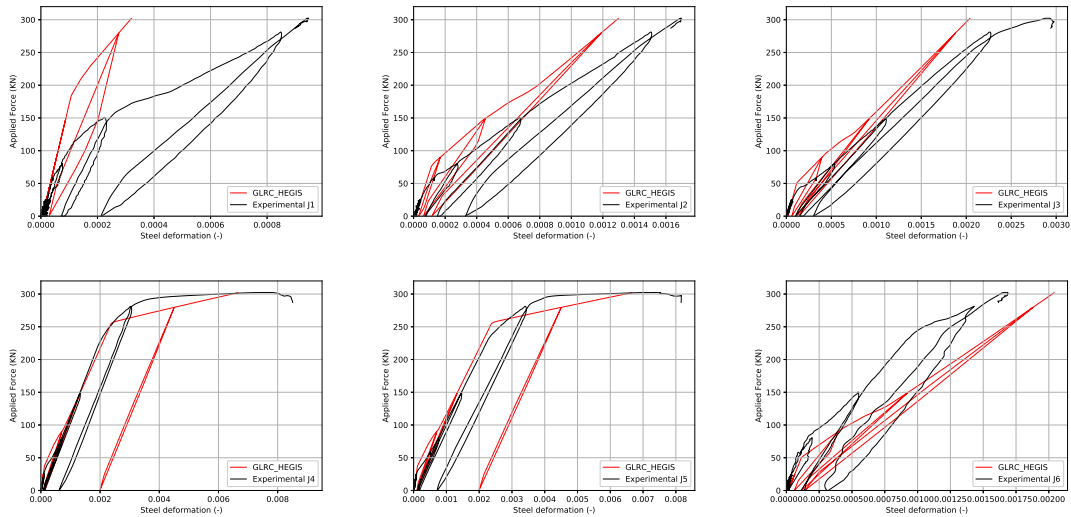


Figure 5.8: Experimental vs. numerical steel deformation given by sensors J1-J6.

As regards the deformation of the steel for sensors J2 and J3, the numerical results lead to an underestimation of the final deformation and to a slightly lower initial drop. The opposite consideration can be done for the J6 sensor. For the sensors J4 and J5 we note that there is an overestimation of the residual plastic steel deformation but with a good approximation in the first phase. The proximity of the J1 sensor to the supports means that the numerical model does not lead to results comparable with the experimental one.

Figure 5.9 (a) shows the trend over time of the main internal variables of the GLRC_HEGIS model. We can note that the Damage of upper layer is larger than that one of lower layer because it's subject to compression and at all times the difference between crack opening and the steel-concrete sliding represent the steel yielding.

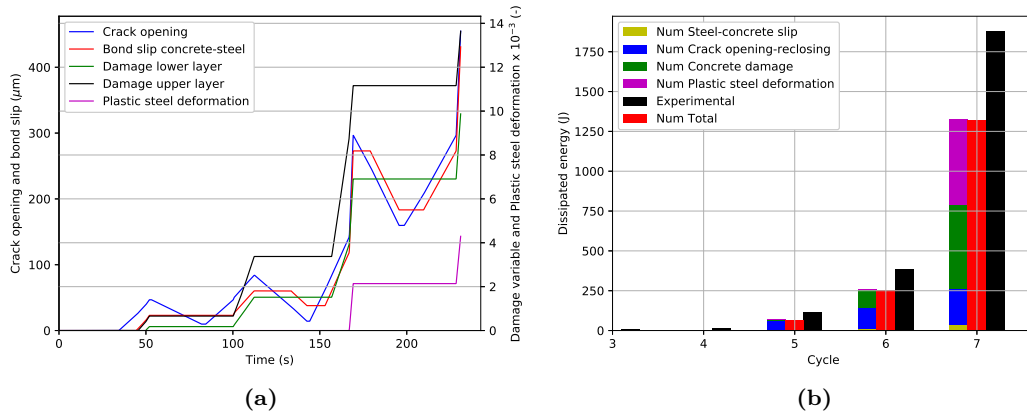


Figure 5.9: Trend of the main internal variables and dissipated energy components.

By analysing instead the components of the dissipated energy (Figure 5.9 (b)) it is noted that in the first elastic phase the energy is dissipated mainly by the concrete damage phenomenon; after the plasticization of the steel, the dissipation of energy is instead governed by the plastic steel deformation. The dissipated energy calculated directly as the internal variable of the model was compared with the experimental one, calculated from the force-displacement curve. The comparison was made for each load cycle up to the penultimate one, since the last cycle only consists of a load phase, it is not possible to calculate the experimental dissipated energy. The figure shows how the numerically calculated dissipated energy is slightly less than the experimental one. This can also be seen through the comparison of the force-displacement curves. The area subtended by the numerical curve is smaller than that subtended by the experimental curve.

5.4 Study of mesh sensitivity

To study the sensitivity of the mesh used, a second model was created consisting of a single element in the direction transverse to the axis. The results, listed below, are perfectly identical to those obtained previously with the first model.

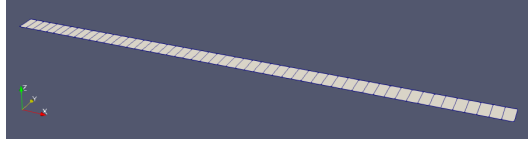


Figure 5.10: Second FE model of the beam.

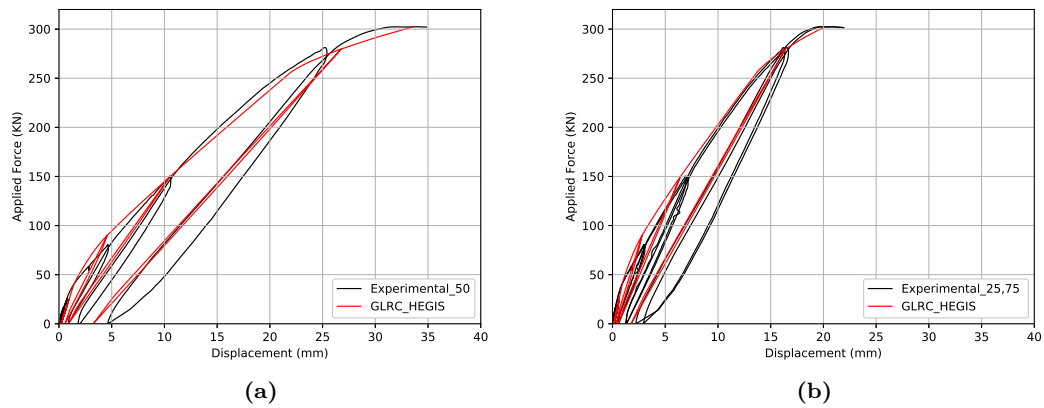


Figure 5.11: Global experimental vs. numerical force-displacement curves at half (a), one quarter and three-fourth of the length (b) for the second model.

The two models lead to exactly identical results because the parameters used are essentially the same. In fact, the parameters that govern the model do not change according to the number of transversal elements (one or two). For simplicity and computational times (slightly less) it is better to use the simpler model. Being used, the latter, only to study the sensitivity of the mesh, in this thesis and in the next sections, reference will always be made to the first model (two transversal elements).

THREE-POINT BENDING TEST ON RC BEAM

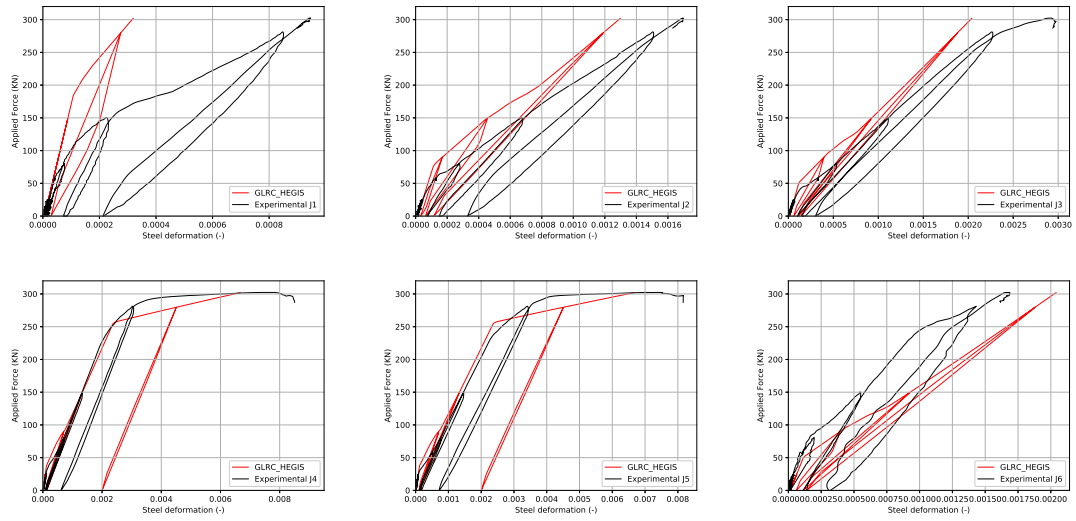


Figure 5.12: Experimental vs. numerical steel deformation given by sensors J1-J6 for the second model.

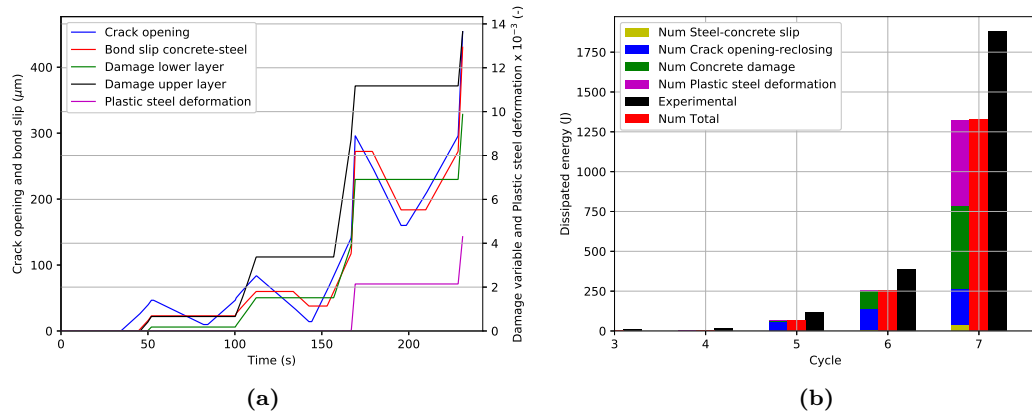


Figure 5.13: Trend of the main internal variables (a) and dissipated energy components (b) for the second model.

5.5 Comparison with membrane behaviour model

A third model has been studied with a different mesh characterized by a membrane behaviour. To better characterize the non-linear parameters of the material, three layers were identified; the upper and the lower having a width equal to twice the distance between the steel bar and the external edge of the concrete. The remainder defines the central layer. To avoid convergence problems the boundary conditions are slightly different from the previous model, in fact the nodes are fixed and the force is applied on the axis of the shell element. All the parameters used for each layer are summarized in the Table 5.4. To underline that all non-linear parameters are equal except for k_0 (for the calculation a σ_d equal to double that of the first model was used) and γ_d (0.2 for the first model and 0.3 for this one). The third FE model of the beam is shown in Figure 5.14

Parameters	Unit	T. layer	C. layer	B. layer
ρ_c	[Kg/m ³]	2350	2350	2350
E_c	[GPa]	37.2	37.2	37.2
ν_c	[-]	0.2	0.2	0.2
E_s	[GPa]	195	195	195
A_{sx}	[cm ² /m]	7.85	0	91.4
A_{sy}	[cm ² /m]	5.03	5.03	5.03
z_{inf}	[mm]	62	62	56
z_{sup}	[mm]	62	62	56
f_{sy}	[MPa]	466	466	466
f_{ct}	[MPa]	2.45	2.45	2.45
G_f	[J/m ²]	62	62	62
α_d	[-]	0.05	0.05	0.05
α_r	[-]	0.05	0.05	0.05
k_t	[-]	0.2	0.2	0.2
T_0	[MPa]	100	100	100
T_1	[GPa/m]	10	10	10
k_0	[Pa]	2050	2050	2050
K_l	[Pa/m]	10 ¹¹	10 ¹¹	10 ¹¹
γ_d	[-]	0.2	0.2	0.2
Φ_x	[mm]	8	0	32
Φ_y	[mm]	8	8	8
s_{rx}	[mm]	121	100	100
s_{ry}	[mm]	120	120	120

Table 5.4: GLRC_HEGIS parameters for RC beam (third model).

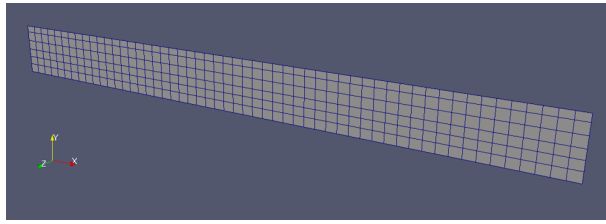


Figure 5.14: Third FE model of the RC beam.

Comparing the results of the two models (first and third) it can be seen that also for the third model (Figure 5.15) there is an underestimation of the residual displacement (the same as the first model). For the curve relative to the central point of the beam, unlike the first model, there is a slightly underestimation of the displacement relative to the peak of the seventh cycle but at the end of the test the numerical displacement and the experimental ones coincide perfectly (Figure 5.15 (a)). For the curve relative to a quarter and three quarters of the length of the beam, there is a slight underestimation of the displacements and a slope slightly greater than the experimental one (Figure 5.15 (b)).

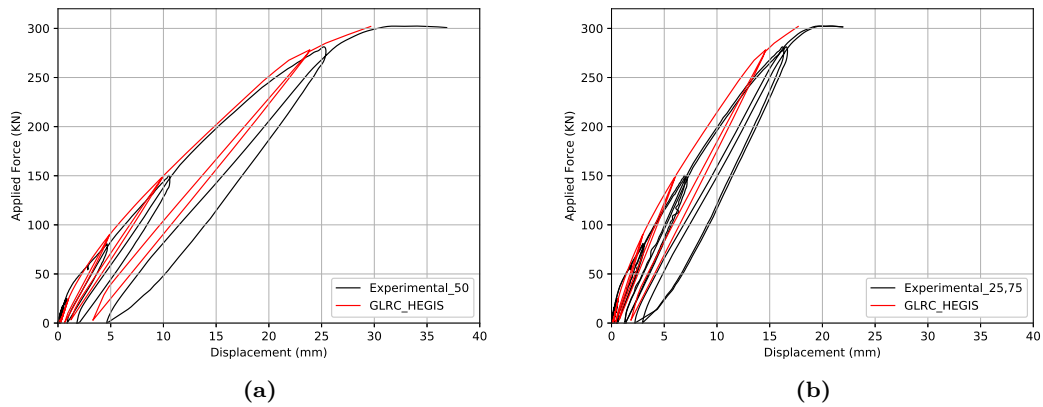


Figure 5.15: Global experimental vs. numerical force-displacement curves at half (a), one quarter and three-fourth of the length (b) for the third model.

Figure 5.16 shows the comparison between experimental and numerical results in terms of steel deformation relative to the third analysed model. The results obtained are in line with those previously seen relating to the first model. The comparison for sensors J2, J3, J4, J5 and J6 is very similar for both models. For the sensors J4 and J5 is also present in this case an overestimation of the residual plastic deformation almost equal to that estimated in the first model. Having modelled the boundary conditions as fixed nodes the results obtained for the sensor J1 are worse than those previously seen. To underline that the sensors J4 and J5 show the plasticization of the steel due to the high deformations reached in the middle of the beam.

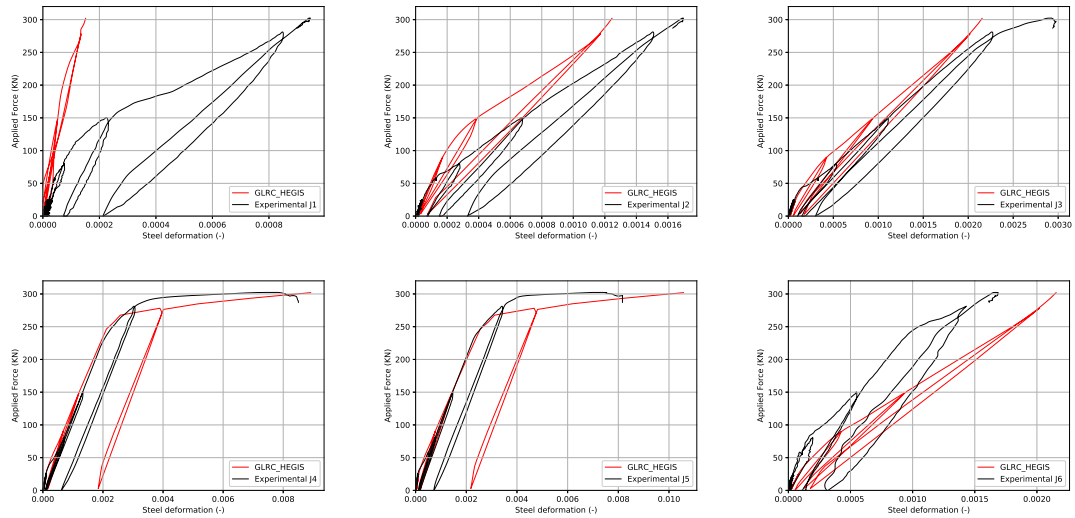


Figure 5.16: Experimental vs. numerical steel deformation given by sensors J1-J6 for the third model.

Analysing the internal variables and the dissipation of energy in the two different models (Figure 5.9 and Figure 5.17), it is noted that the general trend over time is very similar but with slightly higher value of the crack opening in the membrane behaviour model (vertical mesh). As regards the components of energy dissipated, the same considerations made previously are valid. It should be noted that unlike the first model in the figure, the internal variable relating to the damage of the lower layer is not present since, being calculated on the outer edge of the mesh, the compression damage of the concrete is trivially zero. Unlike the first model, there are also differences in the components of the dissipated energy. In this case the numerically estimated dissipated energy is slightly lower than that estimated by the first model because the component of plastic steel deformation is smaller. Also in this case all this can be seen in the comparison of the two force-displacement curves. For the third model the area subtracted from the numerical curve is smaller and in fact the energy dissipated is lower.

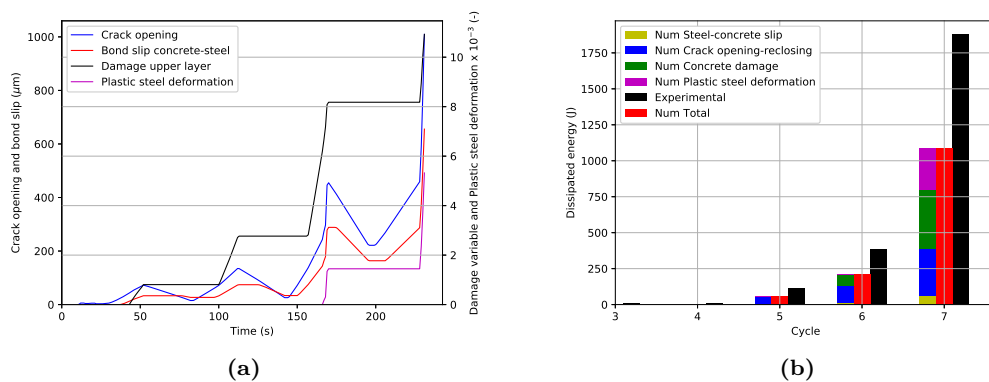


Figure 5.17: Trend of the main internal variables (a) and dissipated energy components (b).

Figures 5.18 5.19 5.20 show the advancement of the crack pattern over loading. The comparison is made between the numerical and the experimental result at 90, 150 and 185 kN, corresponding to the fifth, sixth and seventh load cycles. We note how the numerical results are very close to the experimental ones. For each image, the first figure represents the first model, the second the third and the third the pattern relating to the experimental results. Figure 5.21 shows the numerical values of the crack opening at the end of the test for the first and third model. It should be emphasized that the cracks on the ends of the beam (relative to third model) are due to the application of the boundary conditions in the numerical model.

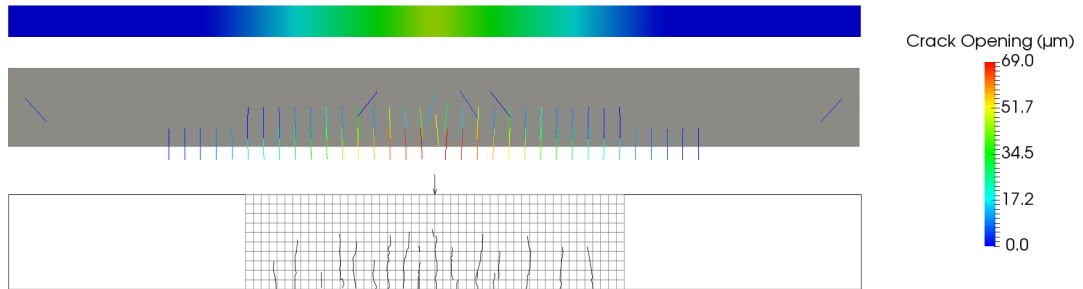


Figure 5.18: Experimental vs. numerical crack pattern at $F = 90$ kN (Cycle 5).

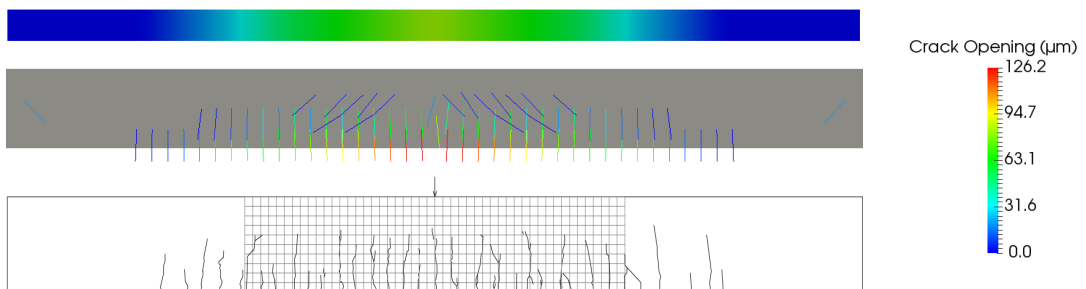


Figure 5.19: Experimental vs. numerical crack pattern at $F = 150$ kN (Cycle 6).

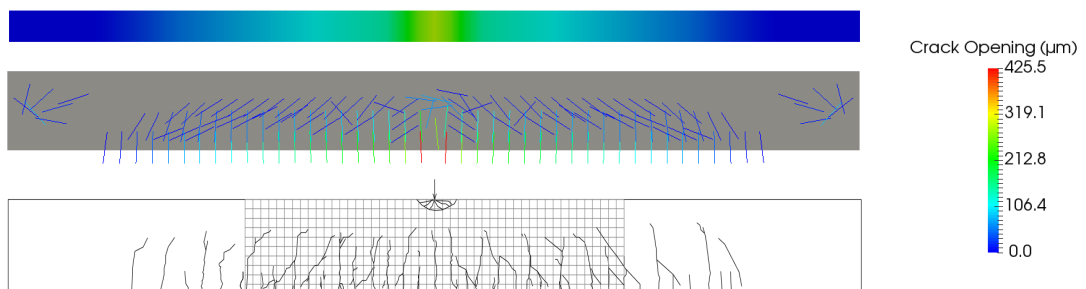


Figure 5.20: Experimental vs. numerical crack pattern at $F = 185$ kN (Cycle 7).

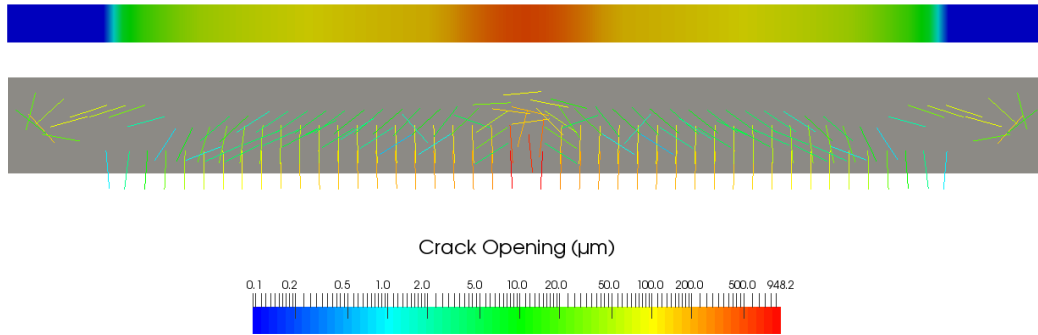


Figure 5.21: Numerical values of the crack openings at the end of test.

Based on the results obtained for the two different models it is possible to draw the following observations:

- The first model better simulates the boundary conditions and the real behaviour of the beam.
- On the other hand for the pure bending behaviour the calibration of the parameters of the GLRC_HEGIS model turns out more complicated.
- The results obtained by the different models are quite similar both in terms of force-displacement curves, both in terms of steel deformation and in terms of dissipated energy.
- The third model allows to obtain many more graphic results also thanks to the functions implemented in it.

Chapter 6

CONCLUSION

This stage allowed me to know and work on the non-linear behaviour of reinforced concrete through the GLRC_HEGIS model, developed at Egis Industries. My work has allowed to improve numerical results already obtained (Chapter 3) and to gain valuable information on the behaviour of the model in the case of pure bending (Chapters 4 and 5). On the basis of the results obtained and described in the previous chapters, it is possible to make the following conclusions:

- Comparing the model with the other global models already implemented in Code_Aster (GLRC_DM and DHRC) it is noted how the taking into account of multiple phenomena not considered by the other global models leads to more complete and better results.
- On a global scale the model describes very well the behaviour of reinforced concrete shell elements and the latter is mainly governed by damage through the model parameter k_0 . At the local scale the lack of some phenomena, not yet considered in the model, leads to results not too far from experimental ones.
- In the case of pure bending, I could see that for some parameters the range of use changes slightly. In particular in my case, the need to have more damage led me to use a value of $\sigma_d = f_c/6$. Future studies for the case of pure bending out of plan could give confirmation and improve the calibration of the parameters.
- For all the models the same non-linear parameters were used except those relating to the damage to the concrete (k_0 and γ_d). This aspect makes it possible to standardize the model and further eliminate the small uncertainty that governs the choice of parameters that must be used.
- Multiple margins for improvement are possible for the model described. The addition of the third family of cracks is being developed by Olivier Lherminier and the case of bending out of plane still requires multiple studies. With the further addition of the concrete permanent strain in compression, more refined and better results will be achieved.

Appendix A

This appendix is devoted to the estimation of the parameters which, even if their physical signification is clear, classical tests do not give enough information to determine them. Some indications about the determination of these parameters are given below:

- In absence of experimental tests values, the fracture energy G_f can be estimated by the expression given by MC10:

$$G_f = 73f_c^{0.18} \quad (\text{A.1})$$

where concrete compressive strength f_c is expressed in MPa and fracture energy G_f in J/m^2

- Parameters α_u and α_r , which define concrete bridging stress cyclic behaviour, may depend on concrete characteristics, especially on the aggregate size and form. If no tests are carried out to identify them, it is recommended to use an unloading slope ratio $\alpha_u \in [0.01, 0.2]$ and crack reclosing ratio $\alpha_r \in [0.01, 0.1]$. It is remarked that when the applied loading creates significant tangential crack displacements w_t , the crack reclosing ratio should be relatively high, in order to reproduce the dilatancy effect, which is not directly considered in the model formulation.
- Aggregate interlock parameters T_0 and T_1 may depend on the aggregate characteristics and the type and magnitude of the loading. Recommend values are $T_0 \in [0.01, 0.1]$ MPa and $T_1 \in [1, 20]$ GPa/m, where the lower bounds of the ranges are related to expected high values of crack opening w_n (or low values of normal concrete stress at cracks) and to cyclic loadings.
- The theoretical average crack spacing of the equivalent tie beams in the x and y directions can be estimated with civil engineering codes formulas for maximum crack spacing, after the transformation to average spacing values by dividing them by 1.7 (for the case of MC10 and EC2). However, it is recommended to use the following optimized formula for average crack spacing:

$$s_{r\alpha} = 1.37c_\alpha + 0.116\Phi_\alpha/\rho_{s\alpha} \quad (\text{A.2})$$

where c_α is the concrete cover of steel reinforcement bars in the α direction. Finally, the experimental values for the the average crack spacing should be used when available.

- The energy release rate threshold k_0 is calculated from the concrete stress at the damage onset σ_d with:

$$k_0 = \frac{(1 - \gamma_d)\sigma_d^2}{2E_c} \quad (\text{A.3})$$

where it is recommended to use $\gamma_d \in [0.2, 0.3]$ for SLS and $\sigma_d \in [f_c/4, f_c/2]$.

- The local bond-slip tangent stiffness can be estimated to $K_l \in [10^{10}, 10^{11}]$ Pa/m, depending on the characteristic values of the obtained steel-concrete slip since it should correspond to the secant stiffness of realistic bond-slip laws as the given by MC10.
- The retained tension stiffening coefficient may vary between $k_t \in [0.1, 0.6]$:
 - $k_t = 0.6$ when calculating crack openings with the same assumptions as MC10 and EC2.
 - $k_t \approx 1/3$ when the computation is done for representing the monotonic mechanical behaviour.
 - $k_t \in [0.1, 0.2]$ when time dependent effects in concrete are important, or in cyclic loadings implying bond degradation.

Appendix B

DEFI_MATER			Values	Explication	Material
ELAS_HEGIS = _F(RHO	=	2500	Density	RC
	ALPHA	=			RC
	AMOR_ALPHA	=			RC
	AMOR_BETA	=			RC
	AMOR_HYST	=			RC
	E_C	=		Concrete Young's modulus	Concrete
	NU_C	=		Concrete Poisson coeff.	Concrete
	E_S	=		Steel Young's modulus	Steel
	A_S (A_SX_SUP, A_SY_SUP, A_SX_INF, A_SY_INF)	=		Steel areas	Shell
	ZINF, ZSUP	=		Position of steel bars	Shell
GLRC_HEGIS = _F(FSY	=		Yielding stress of steel	Steel
	FCT	=		Concrete tensile strength	Concrete
	GF	=		Cracking energy	Concrete
	ALPHD	=	0.01 - 0.2 (0.05 default)	Slope of discharge of concrete traction (fraction of E_C)	Concrete
	ALPHR	=	0.01 - 0.1 (0.05 default)	Crack reclosure (fraction of historical maximum opening)	RC
	SR (SRX_SUP, SRY_SUP, SRX_INF, SRY_INF)	=		Theoretical crack spacing	RC
	K0	=		Threshold of energy dissipation	Concrete
	GAMMD	=	0.2 - 0.3	Asymptotic damage (fraction of E_C)	Concrete
	T0	=	(0.01 - 0.1) MPa	Aggregate interlock threshold	Concrete
	T1	=	(1 - 20) GPa/m	Aggregate interlock slope	Concrete
	KT	=	0.1 - 0.6 (0.33 default)	Coeff. tension stiffening	RC
	KL	=	10 ¹⁰ - 10 ¹¹	Sliding stiffness steel-concrete	RC
	PHI (PHI_XS, PHI_YS, PHI_XI, PHI_YI)	=	10 ¹⁰ - 10 ¹¹	Diameters of the bars	Shell

Table B.1: Parameters of GLRC_HEGIS model.

Internal variable	Meaning	Unit
V1	Normal crack opening, grid 1, top layer	m
V2	Tangential crack opening, grid 1, top layer	m
V3	Normal crack opening, grid 2, top layer	m
V4	Tangential crack opening, grid 2, top layer	m
V5	Steel-concrete slip, X direction, top layer	m
V6	Steel-concrete slip, Y direction, top layer	m
V7	Plastic steel deformation, X direction, top layer	-
V8	Plastic steel deformation, Y direction, top layer	-
V9	Damage variable, top layer	-
V10	Crack spacing, grid 1, top layer	m
V11	Crack orientation, grid 1, top layer	rad
V12	Maximum historical normal crack opening, grid 1, top layer	m
V13	Maximum historical tangential crack opening, grid 1, top layer	m
V14	Crack spacing, grid 2, top layer	m
V15	Crack orientation, grid 2, top layer	m
V16	Maximum historical normal crack opening, grid 2, top layer	m
V17	Maximum historical tangential crack opening, grid 2, top layer	m
V18	Normal crack opening, grid 1, lower layer	m
V19	Tangential crack opening, grid 1, lower layer	m
V20	Normal crack opening, grid 2, lower layer	m
V21	Tangential crack opening, grid 2, lower layer	m
V22	Steel-concrete slip, X direction, lower layer	m
V23	Steel-concrete slip, Y direction, lower layer	m
V24	Plastic steel deformation, X direction, lower layer	-
V25	Plastic steel deformation, Y direction, lower layer	-
V26	Damage variable, lower layer	-
V27	Crack spacing, grid 1, lower layer	m
V28	Crack orientation, grid 1, lower layer	rad
V29	Maximum historical normal crack opening, grid 1, lower layer	m
V30	Maximum historical tangential crack opening, grid 1, lower layer	m
V31	Crack spacing, grid 2, lower layer	m
V32	Crack orientation, grid 2, lower layer	m
V33	Maximum historical normal crack opening, grid 2, lower layer	m
V34	Maximum historical tangential crack opening, grid 2, lower layer	m
V35	Energy (per unit area) dissipated by normal crack opening-closing, grid 1 + 2, sup + inf layer	J/m^2
V36	Energy (per unit area) dissipated by tangential crack opening-closing, grid 1 + 2, sup + inf layer	J/m^2
V37	Energy (per unit area) dissipated by the inelastic steel-concrete slip, X + Y directions, sup + inf layer	J/m^2
V38	Energy (per unit area) dissipated by the plastic steel deformation, X + Y directions, sup + inf layer	J/m^2
V39	Energy (per unit area) dissipated by the compression concrete damage, sup + inf layer	J/m^2
V40	Energy (per unit area) dissipated total (= V35 + V36 + V37 + V38 + V39)	J/m^2
V41	Decrease (both per one) of the membrane stiffness of the plate in RC	-
V42	Decrease (both per one) of the bending stiffness of the plate in RC	-
V43	Stress of steel, X direction, top layer	Pa
V44	Stress of steel, Y direction, top layer	Pa
V45	Stress of steel, X direction, lower layer	Pa
V46	Stress of steel, Y direction, lower layer	Pa
V47	Maximum stress in steels	Pa

Table B.2: Internal variables of the GLRC_HEGIS model.

Bibliography

- [1] EDF. *Open source on www.code-aster.org, Structures and Thermomechanics Analysis for Studies and Research, online documentation. <https://www.code-aster.org/V2/doc/v14/fr/index.php?man=commande>. 1989–2019 (cit. on p. 13).*
- [2] M Huguet. «Homogenised stress resultant constitutive model for cracking in RC plates under seismic loadings». PhD thesis. Ecole Centrale de Nantes, France: Egis industries, Institut de Recherche en Génie Civil et Mécanique, 2016 (cit. on pp. 14, 24, 47, 50).
- [3] M Huguet, M Bourahla, S Erlicher, and P Kotronis. «GLRC_HEGIS global constitutive model for RC walls and slabs for seismic nonlinear structural analyses». In: *Proceedings of the 16th European Conference on Earthquake Engineering*. Thessaloniki, Greece, 2018, pp. 1–12 (cit. on p. 14).
- [4] J Walraven. «Fundamental Analysis of Aggregate interlock». In: *Journal of the Structural Division* 107(11) (1981), pp. 2245–2270 (cit. on p. 20).
- [5] B Li, K Maekawa, and H Okamura. «Contact density model for stress transfer across cracks in concrete». In: *Journal of the Faculty of Engineering, The University of Tokyo* 40(1) (1989), pp. 9–52 (cit. on p. 21).
- [6] P G Gambarova. «Sulla trasmissione del taglio in elementi bidimensionali piani di c.a. fessurati». In: *Proceedings of Giornate AICAP, Bari, Italy, 1983*, pp. 141–156 (cit. on p. 21).
- [7] P Rivillon and A Gabs. «Rapport d’essais 09 26023877 Voile A». In: *CSTB* (2011) (cit. on pp. 25, 26, 33).
- [8] P Rivillon and A Gabs. «Rapport d’essais 09 26023877 Voile B». In: *CSTB* (2011) (cit. on pp. 25, 34).
- [9] P Rivillon and A Gabs. «Rapport d’essais 09 26023877 Voile C». In: *CSTB* (2011) (cit. on pp. 25, 36).
- [10] P Rivillon and A Gabs. «Rapport d’essais 09 26023877 Voile D». In: *CSTB* (2011) (cit. on pp. 25, 37).
- [11] P Bisch, S Erlicher, M Huguet, and G Ruocci. «Experimental and theoretical results on cracking of concrete walls submitted to cyclic shear forces». In: *Proceedings of the 16th European Conference on Earthquake Engineering*. Thessaloniki, Greece, 2018, pp. 1–12 (cit. on p. 27).
- [12] EDF. *SSNS106 – Dégradation d’une plaque en béton armé sous sollicitations variées avec les lois globales GLRC_DM et DHRC.* https://www.code-aster.org/V2/doc/v14/fr/man_v/v6/v6.05.106.pdf. 2019 (cit. on p. 47).
- [13] EDF/ECN. *Poutre_ECN.* https://cheops.necs.fr/fydex/show/Poutre_ECN/. 2002 (cit. on p. 53).